Chapter 4

Synthesis of Noble Metal-Manganese Oxide Nanocomposites and their Applications in Electrocatalysis and Sensing

4.1. Bifunctional Gold-Manganese Oxide Nanocomposites for Water Oxidation and Oxygen Reduction

4.1.1. Introduction

Industrial scale production of clean energy could replace finite fossil fuels with abundant, renewable, environmentally benign energy sources and led to survive the planet in a sustainable way that poses a great challenge to humanity in the 21st century.[1,2] There is a growing need for electrocatalytic water oxidation to give dioxygen for the conversion of electrical energy to stored chemical energy in the form of fuels.[3,4] Plant life is bestowed upon complex catalytic systems for the disintegration of water into its elements; in natural and many protocols designed for artificial photosynthesis, water oxidation, $2H_2O \rightarrow 4H^+ + O_2 + 4e^-$, is a significant step and our understanding of these systems could pioneer in designing effective catalysts.[5,6] The activity of the electrocatalysts for water oxidation is of fundamental importance for the development of promising energy conversion technologies, including, integrated solar water-splitting devices, water electrolyzers, and lithium-air batteries.[7] Therefore, to meet the challenges that lie ahead, water oxidation has become thrust area of research materialistically inspired by the energy challenges and bio-inspired by the emerging understanding of photosystem II.[8,9] The salient features of technical impediment to such a reaction is the need for efficient and inexpensive electrocatalysts capable of oxidizing water to drive this energetically highly unfavourable reaction ($\Delta H° = 572$ kJ/mol).[10] Several protocols have been adopted in the literature to design an efficient, inexpensive and robust electrocatalysts for water oxidation reaction based on metallic platinum,[11] various oxides and complexes of iridium,[12] ruthenium,[13] nickel,[14] cobalt[15] and iron[16] and copper complexes[17] and to evaluate the oxygen evolution activity in acidic and/or alkaline conditions However, amongst the materials considered, so far, for water oxidation catalysts, first row transition metal oxides can offer high earth abundance and reasonable stability in comparison with their noble metal analogues.[18]

Manganese oxides are materials of considerable importance due to their interesting structural, magnetic and transport properties that arise from their outstanding structural flexibility combined with novel chemical and physical properties.[19] Among the series of manganese oxides available in various oxidation states of manganese (II, III, IV),

Mn_3O_4 (hausmannite) has been found to be an effective and inexpensive catalyst in a number of oxidation and reduction reactions.[20] On the otherhand, gold nanoparticles have attracted increasing attention due to their unique properties, such as, high biocompatibility, tuneable electronic and optical behaviour, good conductivity and high catalytic activity, which make them fundamental building blocks for the development of innovative functional materials.[21] The assembly of different nanomaterials with specific optical, magnetic, or electronic properties to multicomponent composites can change and even enhance the properties of the individual constituents.[22] The bifunctional composite nanostructures containing gold have found tremendous importance in the field of nanocatalysis due to rich surface chemistry of gold.[23] The fabrication of nanocomposites containing two or more different functionalities has begun to garner attention for enhanced catalytic properties.[24]

Several reports have been published in the literature using manganese oxides and complexes as electrocatalysts for water oxidation. Dismukes et al.[25] have described the thermodynamic and mechanistic aspects that Nature appears to use to catalyze *in-vitro* water oxidation by photosynthesis using bioinspired and photoactive Mn_4O_4-cubane clusters. Drawing inspiration form these cubane-like CaMn(4)O(x), the biological catalyst found in the oxygen evolving centre in photosystem II, Gorlin and Jaramillo[26] have investigated the electrocatalytic activity of nanostructured manganese oxide surfaces that exhibited similar oxygen electrode activity to the best known precious metal nanoparticle catalysts, *viz.*, platinum, ruthenium and iridium. In a recent communication, Jaramillo and colleagues[27] have demonstrated that addition of Au to MnO_x produces an order of magnitude higher turnover frequency than that of the best pure MnO_x catalysts and a local rather than bulk interaction between Au and MnO_x leads to the observed enhancement in the activity of the reaction. Zaharieva and co-authors[28] have shown that a binuclear manganese molecular complex $[(OH_2)(terpy)Mn(\mu\text{-}O)_2Mn(terpy)(OH_2)]^{3+}$ which is the most prominent structural and functional model of the water-oxidizing manganese complexes operating in plants and cyanobacteria, could be supported on montmorillonite clay and using Ce(IV) as a chemical oxidant, the complex could act as one of the best manganese-based molecular catalyst towards water oxidation. Wiechen et al.[29] have reported the syntheses of layered manganese oxides where the interlayer cations, *viz.*, K-, Ca-, Sr- and Mg-containing birnessites was varied and observed that oxygen-evolving complex require the presence of calcium in their structures to reach maximum catalytic activity. Spiccia

and group[30] have shown that for the nanoparticulates of manganese oxides, formed in Nafion polymer, the catalytic activity towards the water oxidation is dependent on the dispersity of the nanoparticles. They have also reported that the synthetic methodologies for the preparation of highly active mixed valent MnO_x catalysts by partial oxidation of crystalline $Mn^{II}O$ nanoparticles and analysed the catalytic activity in water splitting devices.[31] In a review, the group have elucidated the perspectives of a cluster that contains four manganese and one calcium ions bridged by five oxygen atoms in a distorted chair-like arrangement in the current structural and mechanistic understanding of the oxygen evolving complex in photosystem II.[32] Being inspired by the structural diversity of manganese oxides that occur naturally as minerals in at least 30 different crystal structures, Dismukes and colleagues[33] have chosen to, systematically, compare eight synthetic oxide structures containing Mn(III) and Mn(IV) with cubic phases and concluded that electronically degenerate Mn(III) imparts lattice distortions due to the Jahn–Teller effect that are hypothesized to contribute to structural flexibility important for catalytic turnover in water oxidation at the surface. Suib and group[34] have compared the catalytic activity of mixed valent porous amorphous manganese oxides, cryptomelane-type tunnel manganese oxides and layered birnessite as water oxidation catalysts and observed that amorphous manganese oxides exhibit, significantly, higher turnovers compared to tunnel and layered structures. In spite of all these investigations with molecular and solid-state electrocatalysts, capable of mediating water oxidation, many fundamental questions and practical challenges remain, and improvements are needed in cost, durability and overpotential.

In this sub-section, we have explored the controllable integration into gold-manganese oxide nanocomposites by seed-mediated epitaxial growth at water/*n*-heptane interface and investigated the electrocatalytic activity of the combinatorial catalysts towards water oxidation and oxygen reduction at low overpotential (370 mV) and the, most importantly, under neutral pH condition.

4.1.2. Experimental

4.1.2.1. Synthesis of Gold Nanoparticles

Gold nanoparticles were synthesised by Frens citrate reduction procedure.[35] A standard procedure for the preparation of 10 nm gold nanoparticles is as follows. An aliquot of 50 mL aqueous solution of $HAuCl_4.3H_2O$ (0.25 mM) is heated to boiling and 0.5 mL of

trisodium citrate (1%) is added. In about 25 s, the boiling solution turns faintly blue (nucleation). After approximately 70 s, the blue colour suddenly changes into a brilliant red, indicating the formation of gold particles. The boiling was continued for half an hour and then cooled to room temperature.

4.1.2.2. Synthesis of Gold–manganese oxide Nanocomposites

Gold-manganese oxide nanoparticles have been synthesised at environmentally benign water/*n*-heptane interface under mild reflux condition. In 25 mL binary solvent mixture of water and *n*-heptane (3:1 v/v), 2.5 mM $Mn(ac)_2.4H_2O$ was added and brought to reflux (*ca.* 65-70°C) under stirring. After about 30 min, 150 µL of ammonia was added and immediately after, 1.0 mL of preformed gold nanoparticles (0.25 mM) was added dropwise continuing 10 min to the solution under reflux. The refluxing was continued overall for 1.5 h. After addition of the gold colloid, the colour of the sol was, slowly, begun to change and finally, a brownish red colouration was seen at the end of the reaction. Then, the heating was stopped and the mixture was stirred for 12 h at room temperature. The particles so obtained were retrieved from the solvent mixture by centrifugation at 10,000 rpm for 15 min and were, subsequently, redispersed into water. The dispersion was found to be stable for a month while stored in the vacuum desiccator. Manganese oxide nanoparticles were synthesised following the same procedure devoid of addition of any gold nanoparticles.the particles. A schematic presentation of the synthesis of gold-manganese oxide nanocomposites has been shown in Scheme 4.1.

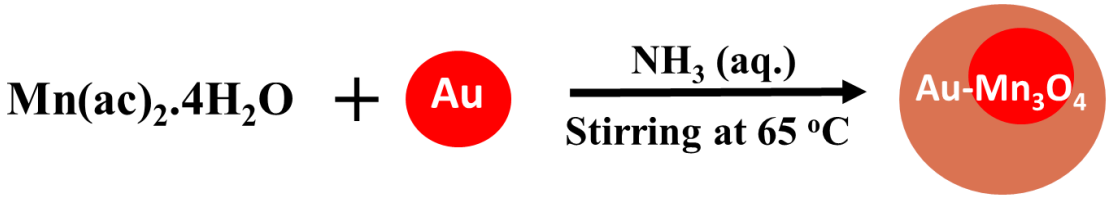

Scheme 4.1. Schematic presentation of the synthesis of Au-Mn_3O_4 nanoparticles

4.1.3. Results and Discussion

In the present experiment, water/*n*-heptane binary solvent mixture plays an important role in the evolution of gold-manganese oxide nanocomposites by epitaxial growth without any external stabilizing agents.[36] The controllable integration of gold and manganese oxide into single nanostructures has been characterised by absorption,

Fourier transform infrared spectroscopy and X-ray diffraction techniques, which reveal the epitaxial growth of manganese oxide on the surface of gold nanoparticles.

4.1.3.1. Absorption Spectroscopy

The absorption spectral features of Au, Mn_3O_4 and Au-Mn_3O_4 particles are presented in Fig. 4.1. Gold nanoparticles exhibit an absorption spectrum with maximum at 520 nm corresponding to the characteristic surface plasmon resonance of conduction electrons of the particles. The electronic absorption spectrum of manganese oxide nanoparticles shows three well-defined regions: the first portion from 250 to 425 nm, the second from 425 to 585 nm and the third one finishing at 700 nm. The first portion is attributed to the allowed $O^{2-} \rightarrow Mn^{2+}$ and $O^{2-} \rightarrow Mn^{3+}$ charge transfer transitions [37] and the last two can be reasonably related to d-d crystal field transitions, $^3E_g(G) \leftarrow {}^3T_{1g}$, $^3A_{2g}(F) \leftarrow {}^3T_{1g}$, $^3A_{2g}(G) \leftarrow {}^3T_{1g}$, $^3T_{2g}(H) \leftarrow {}^3T_{1g}$, $^3T_{1g}(H) \leftarrow {}^3T_{1g}$ and $^3E_g(H) \leftarrow {}^3T_{1g}$, on octahedral Mn^{3+} species.[38] In the spectrum of the nanocomposites, it is seen that the portion of the absorption band due to charge transfer transition of manganese oxide and the surface plasmon band of gold vanishes indicative of strong metal-support interaction.[39]

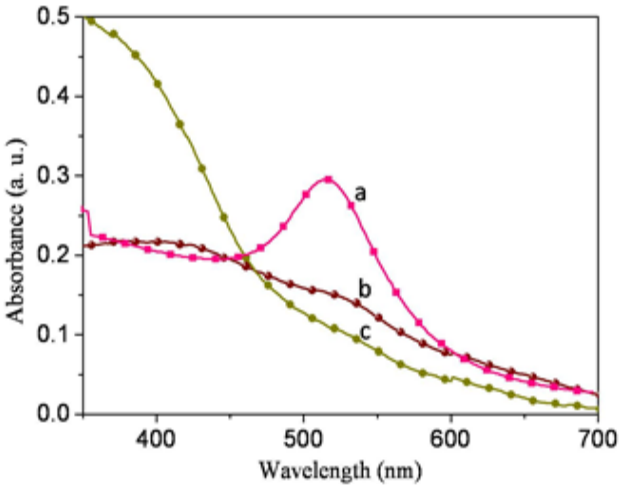

Fig. 4.1. Absorption spectra of (a) Au, (b) Mn_3O_4 and (c) Au-Mn_3O_4 nanoparticles

4.1.3.2. Fourier Transform Infrared Spectroscopy

Fig. 4.2. represents the FTIR spectra of Mn_3O_4 nanoparticles before and after addition of gold nanoparticles. The presence of Mn-O stretching vibrations at 455, 505, 588 and 634 cm^{-1} (trace a) confirms the presence of Mn_3O_4 as the major phase.[40] After the deposition of gold

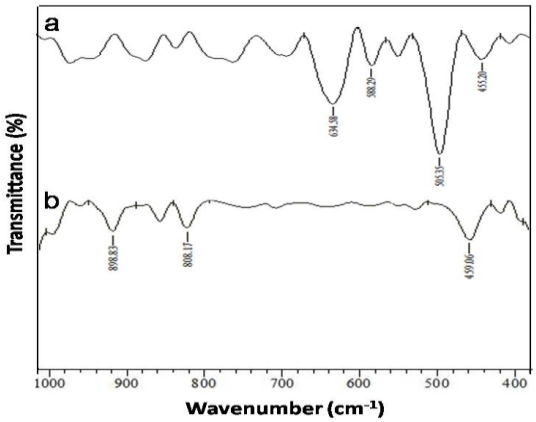

Fig. 4.2. FTIR spectra of Mn_3O_4 (a) before and (b) after addition of gold nanoparticles

nanoparticles (trace b), the band at 455 cm^{-1} is shifted to 459 cm^{-1} and the bands at 505, 588 and 634 cm^{-1} almost vanishes indicating the attachment of gold with the manganese oxide nanostructures.

4.1.3.3. Morphology, Composition and Crystallinity of the Nanocomposites

The morphology, composition and crystallinity of the particles are depicted in Fig. 4.3. Transmission electron micrographs (panel a, b, c) of gold, manganese oxide, gold-manganese oxide show that the particles are of 10±2, 15±3 and 20±5 nm, respectively. In the image of the nanocomposites, the Au particles appear black and Mn_3O_4 are light coloured because Au has a higher electron density and allows fewer electrons to transmit.[19] Dark field scanning tunneling electron micrographs (DF-STEM) (panel d)

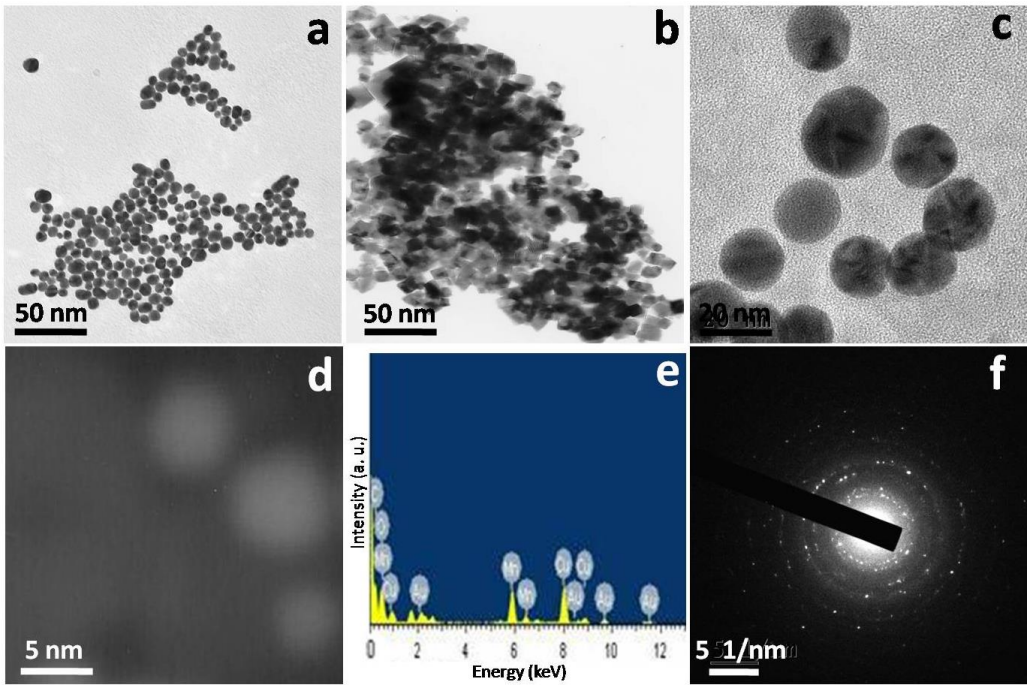

Fig. 4.3. (a, b, c) Transmission electron micrographs of Au, Mn_3O_4, and Au-Mn_3O_4 nanoparticles respectively; (d) dark field scanning tunneling electron micrographs, (e) energy dispersive X-ray, and (f) selected area electron diffraction pattern of Au.

points out the epitaxial growth of manganese oxide on gold nanoparticles. The energy dispersive X-ray spectrum (panel e) of Au-Mn_3O_4 particles reveals that the particles are composed of Mn, C, O, Cu and Au elements. Among those elements, the signals of Mn, O and Au result from the Mn_3O_4 and Au particles which form the product and the signals of C, O and Cu elements come from the precursor and the supporting TEM grid. From the SAED pattern of the composites, it is clear that a bright reflection appears from the (111) plane of fcc structured gold and a strong ring pattern corresponding to (101), (103) and (211) planes of tetragonal hausmannite structure. In addition, a

combined multireflection results due to Au-Mn_3O_4 composite formation, confirming the crystallinity of the resultant materials.[19]

4.1.3.4. X-ray Diffraction Pattern

X-ray diffraction pattern of Au-Mn_3O_4 is shown in Fig. 4.4. On the basis of the position and relative intensity, all diffraction peaks could be indexed to standard fcc structured Au and tetragonal hausmannite structure of Mn_3O_4 nanoparticles with lattice parameters a = b = 5.762 Å, and c = 9.469 Å and space group $I4_{1/amd}$, which are consistent with the standard values of bulk Mn_3O_4 (JCPDS# 24-0734).[41]

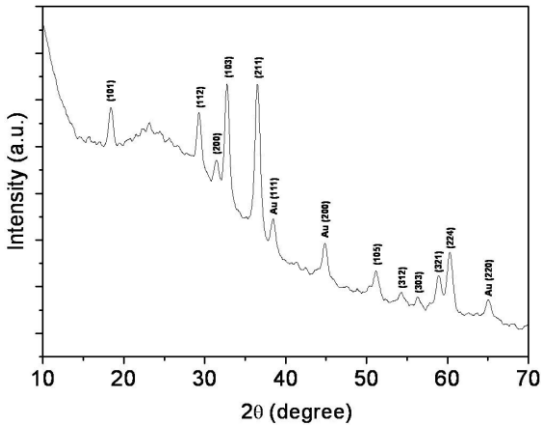

Fig. 4.4. X-ray diffraction pattern of Au-Mn_3O_4

4.1.3.5. Modification of the Gold Electrodes for the Study of Electrocatalytic Activity

Now a days, Au, Mn_3O_4 and Au–Mn_3O_4 nanoparticles are employed to investigate the electrocatalytic activity toward the water oxidation reaction. To investigate the electrocatalytic activity, the gold electrode was modified as described below. At first, the gold electrode was polished with 0.05 μm alumina powder on a polishing microcloth and rinsed, methodically, with distilled water. The mechanically cleaned electrode was decontaminated electrochemically in 1.0 M H_2SO_4 solution.

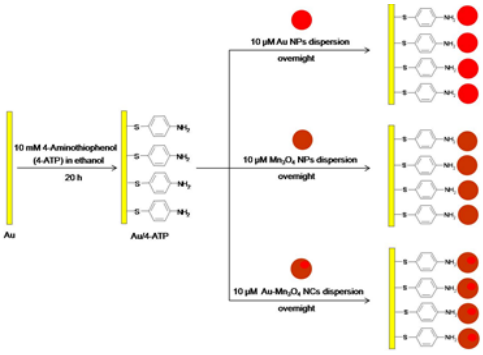

Scheme 4.2. Modification of the gold electrode with Au, Mn_3O_4 and Au-Mn_3O_4 nanoparticles.

A reproducible cyclic voltammogram between -0.2 to +1.5 V *vs.* Ag/AgCl electrode ascertained the cleanliness of the electrode. The electrode was, then, soaked with distilled water and subsequently, dipped in 10 mM 4-aminothiophenol (4-ATP) solution for 20 h to allow the formation of self-assembled monolayer (SAM) over gold surface. After that, the 4-ATP functionalized gold electrode was washed thoroughly with

distilled water and placed in 10 μM colloidal dispersion for the desired period to obtain the nanoparticles-modified electrode. The modification of the gold electrode with the nanoparticles is shown schematically in Scheme 4.2.

Electrochemical impedance spectroscopy of 1.0 mM $[Fe(CN)_6]^{3-/4-}$ in 0.1 M PBS at bare, 4-ATP modified and NPs or NCs-immobilized gold electrode is shown in Fig. 4.5. It is seen that the charge transfer resistance (R_{CT}) is very high when the gold electrode surface was modified with self-assembled monolayer (SAM) of 4-ATP (brown) than bare gold (black). The electronic communication between the redox species $[Fe(CN)_6]^{3-/4-}$ in solution and the underlying gold electrode becomes restricted due to formation of SAM. After the immobilization of NPs on 4-ATP/gold electrode, the R_{CT} decreased indicating that the NPs were, successfully, immobilized on the 4-ATP modified gold electrode and a good electronic communication was attained between the redox species $[Fe(CN)_6]^{3-/4-}$ in solution and the underlying Au electrode through NPs.

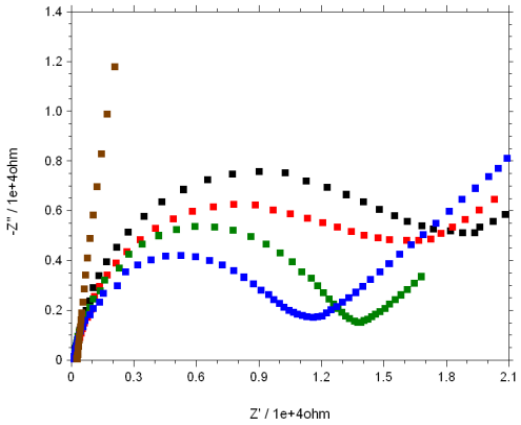

Fig. 4.5. Overlaid Nyquist plot ($-Z''$*vs.*Z') for 1.0 mM $[Fe(CN)_6]^{3-/4-}$in 0.1 M PBS (pH 7.5) at bare gold (black), 4-ATP/gold (brown), Au NPs/4-ATP/gold (red), Mn_3O_4NPs/4-ATP/gold (green) and Au-Mn_3O_4NCs/ATP/gold (blue) electrodes, where, anodic current amplitude, E_{ac} = 10 mV while the frequency varies from 0.01 - 100000 Hz.

4.1.3.6. Electrocatalytic activity towards Water Oxidation Reaction (WOR)

In the Fig. 4.6. cyclic voltammogram of 4-ATP/gold (red), Au NPs/4-ATP/gold (green), Mn_3O_4 NPs/4-ATP/gold (blue) and Au-Mn_3O_4 NCs/4-ATP/gold (black) electrodes in PBS at pH~7.5. A particular amount (20 μg) of the catalysts was dissolved in 10 mL of water in each case. These dispersions were, then, employed for the loading of catalysts by dipping the electrodes and allowed to equilibrate overnight under vacuum. It is observed that Au-Mn_3O_4 nanocomposites (black) causes a shift of oxidation potential in the less positive potential and a large increase of current height compared to that of only Au (green) or Mn_3O_4 nanoparticles (blue). In spite of an ideal electrocatalytic process at

its thermodynamic potential (for example, at 0.62 V *vs*. Ag/AgCl, pH ~7.0 and 1 atm O_2), the actual electrode reaction occurs at a more positive potential (i. e., overpotential) whose magnitude reflects the electrode kinetics of the solution. It is seen that Au NPs/4-ATP/gold, Mn_3O_4 NPs/4-ATP/gold and Au-Mn_3O_4 NCs/4-ATP/gold electrode displays anodic response at +1.13 V ($\eta \approx 0.51$ V, pH~7.5) , +1.12 V ($\eta \approx 0.50$ V, pH~7.5) and +0.998 V ($\eta \approx 0.37$ V, pH~7.5) *vs.* Ag/AgCl, respectively in the potential window 0.3 - 1.3 V signifying water oxidation in 0.1 M PBS (pH ~ 7.5) and the corresponding cathodic peak at ~ + 0.5 V for $O_2 + 4H^+ + 4e \rightarrow 2H_2O$ at the pH~7.5 indicative of the reversibility of the process,[3] whereas no such signal appeared for 4-ATP/gold electrode. It was noted that the particles synthesized, in the present experiment, are stable for a couple of weeks without any significant agglomeration or precipitation of the particles. After the deposition of the particles at the electrodes, the catalytic activity of the particles was measured and the electrodes were rinsed in distilled water after the experiments. It was noted that the electrodes retain their catalytic activity even after 48 h of the loading of the catalysts. Therefore, it could be conceived that the particles do not suffer from dissolution or corrosion during the time of measurement of their electrocatalytic activity. However, assuming that the particles are nearly spherical and the density of Mn_3O_4 and Au-Mn_3O_4 as 4.86 and 12.09 g cm^{-3} (taking an average of the density of Au and Mn_3O_4) respectively, the number of Mn_3O_4 and Au-Mn_3O_4 particles is *ca.* 2.3×10^{12} and 3.8×10^{11} respectively and the corresponding surface area is *ca.* 1625×10^{12} and 477×10^{12} nm^2, respectively.[42] Therefore, it is evident that Au-Mn_3O_4 composites are better electrocatalysts than the Mn_3O_4 particles.

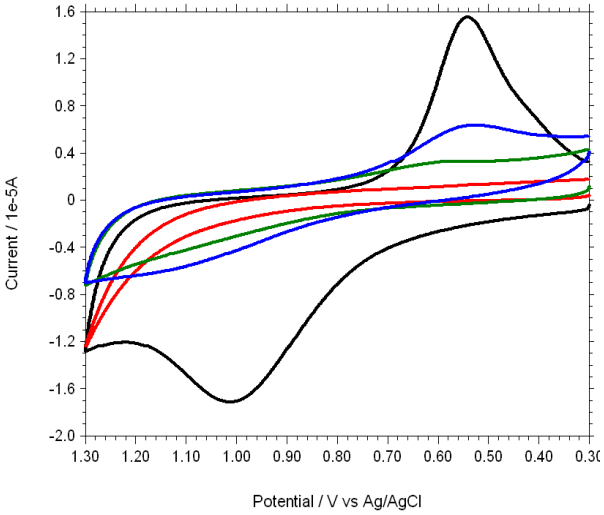

Fig. 4.6. Cyclic voltammograms of water oxidation in presence of 4-ATP/gold (red), Au NPs/4-ATP/gold (green), Mn_3O_4 NPs/4-ATP/gold (blue) and Au-Mn_3O_4 NCs/4-ATP/gold (black) electrodes in PBS at pH~7.5.

The turnover frequency (TOF) of the catalysts could be calculated using the equations[43]:

$$I_{cat} = nFAk_{cat}\Gamma_{cat} \quad (4.1)$$

$$\Gamma_{cat} = Q/nFA \quad (4.2)$$

where, I_{cat} is the catalytic current density, n the moles of electron transfer, F the Faraday constant, A the geometric surface area of the underlying anodic surface, k_{cat} the rate constant of the electron transfer, Γ the surface coverage in moles per square centimeter and Q the charge obtained by integrating the cathodic peak (= $\int i_f\,dt$, where i_f is Faradaic current). From eqn. (1) and (2), we can estimate the electroactive site turnover rate during O_2 evolution as,

$$k_{cat} = I_{cat}/Q \quad (4.3)$$

The catalytic current density for Au, Mn_3O_4 and Au-Mn_3O_4 is 3.8, 5.8 and 17.4 μA, respectively and the charge obtained by integrating the cathodic peak for Au, Mn_3O_4 and Au-Mn_3O_4 is 2.4, 2.6 and 3.8 μC, respectively. Therefore, the turn-over frequency corresponding to Au, Mn_3O_4 and Au-Mn_3O_4 is calculated to be 1.6, 2.2, and 4.6 s^{-1}, respectively. However, the concept of turn-over frequency is based on the number of the active sites of the catalysts. In the above equations, the active sites have been replaced as surface area, which is an apparent value; therefore, the calculated TOFs provide only apparent values rather than the real TOFs of the catalysts. In addition, for the catalyst of Au-Mn_3O_4, the active sites for Au are different from that for Mn_3O_4 but also bring unique collective and combined effect and as a result, the calculated TOF is an average of the constituent particles. The catalytic activity for water oxidation was perceived for Au-Mn_3O_4 nanocomposites as compared to their individual counterparts as those not only combine the properties of both noble metal and metal oxides, but also bring unique collective and synergistic effect in comparison with single component materials.[27,44]

4.1.3.7. Study of Water Oxidation Reaction with Different Sizes of the Gold Nanoparticles in the Composites

To study the efficacy of the electrocatalytic activity of the gold-manganese oxide nanocomposites, three different sizes of gold nanoparticles (*viz.*, 10, 16, and 25 nm by varying [Au(III)]/[citrate] ratio as 5.0, 3.5, and 2.5 respectively) prepared by Frens' citrate reduction procedure were employed for the preparation of gold-manganese oxide nanocomposites and their electrocatalytic activity was studied towards oxygen reduction reaction. It is seen that Au(10)-Mn_3O_4 are more efficient catalysts for water oxidation reaction than Au(16)-Mn_3O_4 and Au(25)-Mn_3O_4 composites (Fig. 4.7.) These study elicite the reproducibile electrocatalytic activity of the nanocomposites. Therefore, it could be conceived that Au-Mn_3O_4 composites are more efficient catalysts for water oxidation reaction than the individual Au or Mn_3O_4 nanoparticles. The enhanced catalytic activity of the Au-Mn_3O_4 catalysts could be attributed to the beneficial presence of higher amount of oxidizable gold species and surface oxygen vacancies resulting from the strong interaction between Au and the reactive surface of Mn_3O_4 nanoparticles.[45] An increase in 5d vacancy of Au increases the interaction of O_2 and Au, thereby, enhancing the catalytic activity of Au in the composites.[46]

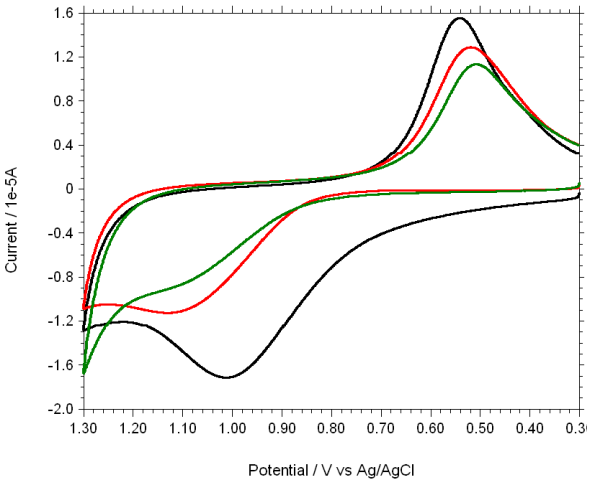

Fig. 4.7. Cyclic voltammogram for the water oxidation at Au(10)-Mn_3O_4 (black), Au(16)-Mn_3O_4 (red) and Au(25)-Mn_3O_4 (green)-modified gold electrode in 0.1 M PBS at pH~7.5.

4.1.3.8. Electrocatalytic Activity towards Oxygen Reduction Reaction (ORR)

However, interestingly, it was noted while the electrode was cycled to cathodic potential after several scan through the catalytic anodic wave, an irreversible peak was observed at *ca.* - 0.001 to - 0.2 V for different modified electrode

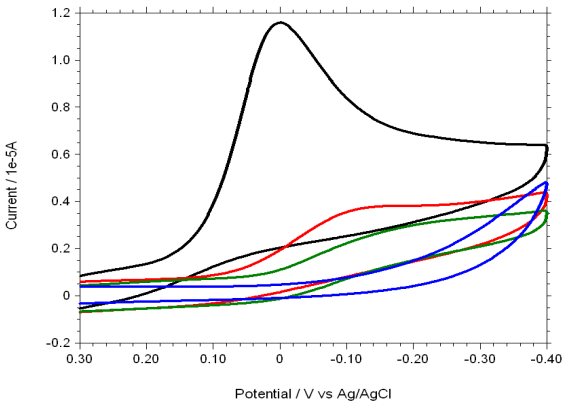

Fig. 4.8. Cyclic voltammograms for oxygen reduction in the presence of 4-ATP/gold (blue), Au NPs/4-ATP/gold (green), Mn_3O_4 NPs/4-ATP/gold (red) and Au-Mn_3O_4 NCs/ATP/gold (black) electrodes in PBS at pH~7.5.

systems as presented in Fig. 4.8. This peak could be attributed to O_2/O_2^- couple[47] and indicates that O_2 was evolved from water oxidation on the electrode surface.

4.1.3.9. Simultaneous Oxygen Reduction Reaction during Water Oxidation

A digital camera photograph showing the evolution of oxygen gas during water oxidation and the corresponding cyclic voltammogram of Au-Mn_3O_4 NCs/4-ATP/gold electrodes in normal and N_2-saturated PBS at pH~7.5 are shown in Fig. 4.9. Under ambient condition the current height due to oxygen reduction is higher than N_2-sparged solution, which authenticates that the origin of this peak is originated due to O_2 reduction. In a like-wise manner of water oxidation, the higher cathodic peak current and lower reduction potential at Au-Mn_3O_4 NCs (black) than Mn_3O_4 NP (red) and Au NPs (green)- modified gold electrodes authenticate that the Au-Mn_3O_4 are better ORR catalysts than the individual Au or Mn_3O_4 particles.[42] The Au-Mn_3O_4 particles upon exposure to oxygen form radical species on the surface of the catalysts. The ability to form such radical species in the presence of oxygen leads to enhanced performance of the Au-Mn_3O_4 composites in the oxygen reduction reaction.[48] It is also likely that oxygen can dissociate on the Au surface and spill over from Au to the oxygen vacancies in the oxide, which synergistically promotes the adsorption and dissociation of O_2.[49] Therefore, the different surface structural features clearly determine the strength of metal-support interaction and thus the catalytic activity. The overpotential for Au, Mn_3O_4 and Au-Mn_3O_4 is 514, 505 and 370 mV, respectively. When Au interacts with transition metal oxides to form a reduced oxide and an oxidized metal at the interface of

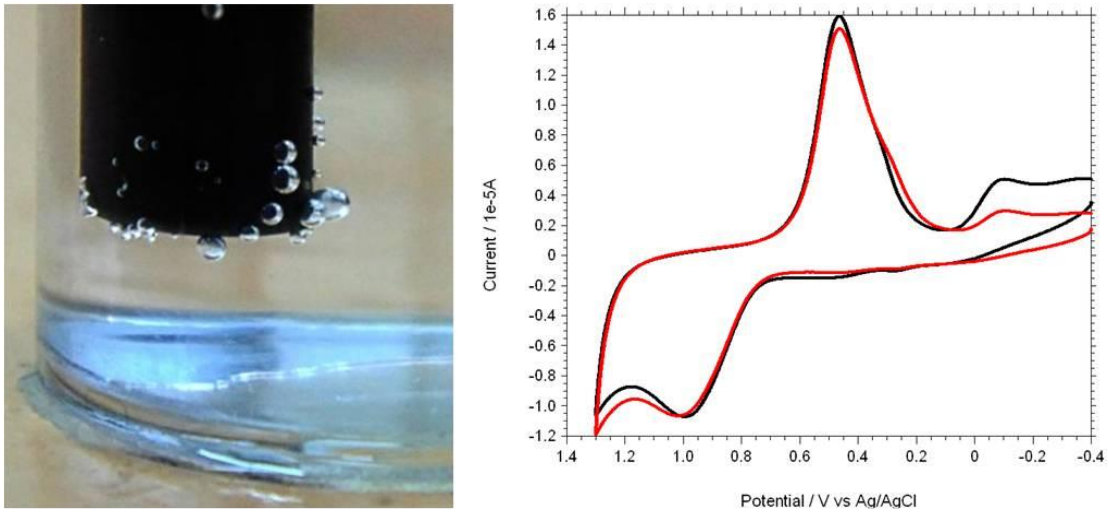

Fig. 4.9 (left) Digital camera photograph showing oxygen gas evolution during water oxidation reaction; (right) cyclic voltammogram of oxygen reduction of Au-Mn_3O_4 NCs/4ATP/Au electrodes under ambient (black) and N_2-saturated (red) PBS at pH~7.5.

the two materials,[50,51] it dissolves at an oxidizing potentials relevant to the water oxidation reaction.[52] Therefore, the presence of Au during the water oxidation reaction could lead to an enhancement in the electrocatalytic activity of Mn_3O_4 particles.

The oxidation of water to dioxygen is one of the key reactions that need to be fully understood in order to apply to water splitting devices. A reasonable mechanism for the water oxidation and oxygen reduction reactions on the nanocomposite surface could be enunciated as follows. From an electrochemical perspective, this reaction can be divided in two half reactions, water oxidation and proton reduction.[53] The formation of H_2O_2 from such species suggests that hydrolysis of an O–O bonded species proceeds more rapidly than the additional oxidation steps needed to form O_2. In the presence of the catalysts, an O–O bonded intermediate, can undergo rapid electron transfer in the material or to the electrode to enable selective evolution of O_2. In the present experiment, upon addition of gold to the metal oxide system, gold-metal oxide perimeter interface acts as a site for activating the reactants. Therefore, it could be conceived that very strong metal–support interactions after Au deposition,[54] creates a unique interface and that results in enhanced activity for water oxidation and oxygen reduction reactions.

Cyclic voltammetric data of water oxidation and oxygen reduction in presence of the nanomaterials are summarized in Table 4.1. The overpotential of different manganese-based systems as a function of experimental conditions has been discussed elsewhere.[27] Fig. 4.10 illustrates the cyclic voltammograms at varying pH of the PBS with Au-Mn_3O_4 NCs/4-ATP/Au electrode. A little change of current height was observed for O_2/O_2^- couple at -0.18 V but the anodic peak potential as well as peak current varied with the change in pH of the solution (Fig. 4A). A plot of potential *vs.* pH and current *vs.* pH (Fig. 4B) show that the potential is optimum at pH~7.5 and the electrocatalytic activity for water oxidation increases with increasing pH (5.5 - 9.5) of the solution, respectively.

Table 4.1. Cyclic voltammetry data of water oxidation and oxygen reduction in presence of nanomaterials

Catalysts	water oxidation potential ($E_{ox,\ H2O}$),V	I_{pa}# (μA)	1st oxygen reduction potential ($E_{red,\ O2}$), V	$I_{pc\ (1)}$# (μA)	2nd oxygen reduction potential ($E_{red,\ O2}$), V	$I_{pc\ (2)}$# (μA)
Au	1.134	-4.5	0.562	3.3	-0.189	2.9
Mn_3O_4	1.125	-6.8	0.515	6.3	-0.139	3.8
Au-Mn_3O_4	0.998	-17.1	0.546	15.6	-0.001	11.6

where, I_{pa} and I_{pc}denote the irreversible peak currents at anode and cathode, respectively.

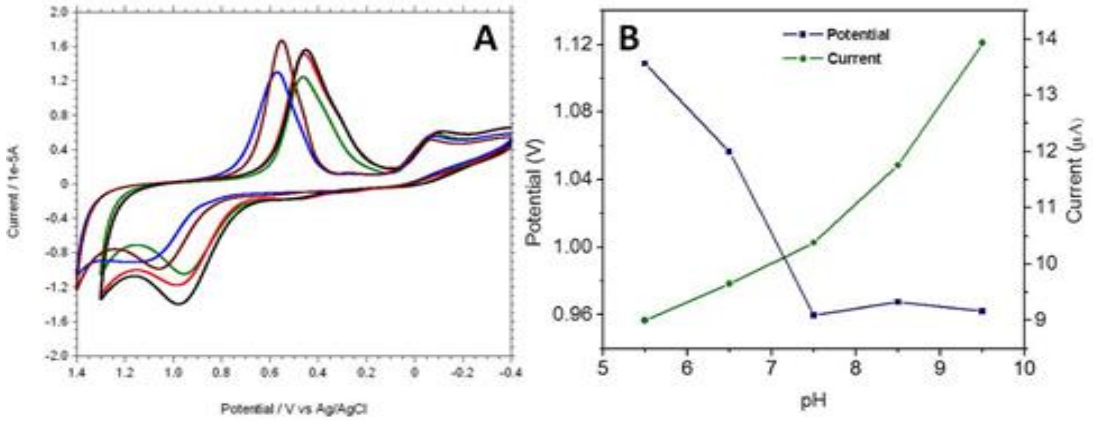

Fig. 4.10 (A) Cyclic voltammograms of water oxidation in 0.1 M PBS at pH~5.5 (blue), 6.5 (brown), 7.5 (green), 8.5 (red), 9.5 (black) with Au-Mn_3O_4 modified electrodes; and (B) Profile showing the variation of current and potential as a function of pH.

A comparative account of the pH condition of the experiment and overpotential of the Au-Mn_3O_4 and some other electrocatalysts is presented in Table 4.2.

Table 4.2 A Comparative Account of the pH Condition of the Experiment and Overpotential of the Au-Mn_3O_4 and some other Electrocatalysts

Catalyst	**pH**	**Overpotential (mV)**	**References**
IrO_x	13.0	290	Murray et al.[Ref. 12]
Nickel Film	14.0	1070	Dai et al. [Ref. 14]
$Co(III)_3Co(IV)O_4$	9.5	350-430	Britt et al. [Ref. 15]
Copper-bipyridine	11.8-13.3	750	Mayer et al. [Ref. 17]
Au-Mn_3O_4	7.5	370	Present Work

4.1.4. Conclusion

In conclusion, the synthesis of stabiliser-free gold-manganese oxide nanocomposites by seed-mediated epitaxial growth employing environmentally benign water/*n*-heptane interface paves a facile strategy through surface attachment for combinatorial catalyst design. We have, successfully, overcome the key challenge of recent research of electrocatalytic water oxidation, surprisingly, at nearly neutral pH (pH~7.5) and low overpotential of 370 mV which is beyond the typical range of many homogeneous water oxidation catalysts (600 – 900 mV). As manganese oxides are available in various oxidation states and exhibit extensive biomimetic chemistry with oxygen, this result adds a new feather and illuminates ample opportunities in water oxidation electrocatalysis using wide varieties of inexpensive and earth-abundant materials. This facile and environmentally benign synthetic strategy for the nanocomposites could be upscaled at the industrial level and may offer a promising future for renewable energy technologies.

4.2. Mn_3O_4−Ag Nanocomposites for Sensing of Volatile Organic Compounds

4.2.1. Introduction

Volatile organic compounds (VOCs) are carbon based chemicals present in the atmosphere and play a significant role in tropospheric chemistry.[55] It has been experienced that the toxicities inherent in volatile organic compounds arising due to their various specific chemical reactivities can affect the regional as well as global environment[56] and may cause adverse health hazards, including, the potential cause of cancer.[57-58] Therefore, on-site and real-time detection of VOCs in the gas phase has received global attention to overcome the challenges for environmental management, process control, and medical diagnosis of human health.[59-61] The advancement of the sensor technology has been utilised as a solution to this problem; during the past several decades,VOC detection systems have been manufactured as bioinspired artificial olfactory systems, known as "electronic noses", composed of an array of partially selective chemical sensors conjugated with pattern recognition elements for the selective and sensitive analysis of simple as well as complex gas mixtures.[62,63] It is seen that sensory elements contained within the electronic nose systems are capable of transforming chemical information into an output signal, and individual elements in the array can exhibit the concentration- and target-specific interactions that provide a versatile approach to chemical analysis of the VOCs.[64] However, to meet the growing number of clinical challenges, the advent of maneuvering new diagnostic and detection technologies have focused on nanomaterial-based sensors for the detection of VOCs. During the last few years, organic [65-68]and inorganic[69-72] and inorganic-organic hybrid[73]nanoscale semiconductors with wide band gaphave received increased attention because of their high sensitivity and selectivity towards the detection of VOCs. Metal oxide semiconductors, such as, SnO_2,In_2O_3, TiO_2, ZnO, CuO, WO_3 and their composites,[74-81]have, often, been exploited as sensing materials of these harmful organic compounds at low concentrations. Noble metal (Ag, Au, Pd and Pt) nanoparticles have, sometimes, been doped or decorated into/on the metal oxide components to improve the sensitivity and selectivity of the desired sensing event.[82-85]Considering the earth

abundance and biogeneticity, Mn_3O_4 has received a great deal of attention as the model spinel compound due to its unique physical, chemical and structural properties.[86] Bulk Mn_3O_4 is a *p*-type semiconductor with a wide direct bandgap of 2.3 eV and is the stablest among the manganese oxides available in their various oxidation states.[87] On the other hand, silver particles, in the nanometer size regime, upon conjugation to well-engineered supporting materials, can act as active catalysts in specific reactions.[88] While the synergistic properties of the manganese oxide/silver conjugates have been examined in catalytic ethanol oxidation,[89] for improving battery performance,[90,91] to study their oxygen reduction properties,[92]and for the fabrication of high-performance microsupercapacitors,[93,94] have been exploited the detection and determination of volatile organic compounds in this investigation.

In this sub-section, the synthesis of Mn_3O_4−Ag nanocomposites has been described by seed-mediated epitaxial growth of manganese oxide by alkaline hydrolysis of precursor salt on the surface of silver nanoparticles at the water/*n*-heptane interface. The morphology of the nanocomposites has been varied by employing different sizes of silver nanoparticles in the reaction mixtures. The as-synthesised particles have been characterised by absorption spectroscopy, diffuse reflectance spectroscopy, transmission electron microscopy, high resolution transmission electron microscopy, Fourier transform infrared spectroscopy, Raman spectroscopy, X-ray diffraction pattern, cyclic voltammetry, selective area electron diffraction pattern, energy dispersive X-ray analysis, elemental mapping and thermogravimetric analysis. These nanocomposites of varying composition have been found to serve as efficient sensors for various hazardous volatile organic compounds, exhibiting high sensitivity and selectivity to ethanol. The differences in the structure-function relationship of the Mn_3O_4−Agupon variation of the size of silver particles towards the sensory activity of VOCs have been elucidated.

4.2.2. Experimental

4.2.2.1. Synthesis of Silver Nanoparticles

Monodispersed silver nanoparticles of five different sizes have been synthesised by wet chemical reduction of silver nitrate using sodium borohydride as the reducing agent and trisodium citrate as the reducing agent as well as the capping agent by modification of the Frens' citrate reduction method.[35] In a typical experiment, 50 mL of 0.25 mM silver

nitrate solution was taken in a 100 mL beaker. Then, 2.5 mL 1% trisodium citrate solution was added and stirred vigorously using a magnetic stirrer at 0 ^{0}C temperature. After that, approximately, 1 mL of freshly prepared sodium borohydride solution ($AgNO_3$:$NaBH_4$ = 1: 20) was added to the reacting solution at a time and stirring was continued for another 30 min. At this temperature, trisodium citrate does not reduce the silver nitrate solution and only acts as stabilizing agent. The development of yellow coloration indicates the formation of silver nanoparticles. In this method, it is possible to control the size of the particles by varying [$AgNO_3$]/[$NaBH_4$] ratio during the reduction step. However, a lexicon of the synthetic conditions for the preparation of five different sizes of silver nanoparticles has been enunciated in Table 4.3.

Table 4.3. Synthetic Conditions for the Five Different Sets of Silver Nanoparticles[#]

Set	Vol. of $AgNO_3$ (1mM) (mL)	$AgNO_3$:$NaBH_4$	Vol. of Citrate (1%) (µL)	λ_{max} (nm)	Color	Particle Size (nm)
1	2.0	1.0:20	2000	384	Faint Yellow	2±0.5
2	2.0	1.0:20	1500	391	Yellow	5±0.9
3	2.0	1.0:20	1000	395	Yellow	10±2.0
4	2.0	1.0:20	500	399	Greenish Yellow	15±2.6
5	2.0	1.0:20	200	404	Brownish Yellow	20±3.0

[#]For silver nanoparticle synthesis, the total volume of the solution was 50 mL.

4.2.2.2. Synthesis of Mn_3O_4−Ag Nanocomposites

In a typical environmentally benign synthesis of the nanocomposites, an aliquot of 0.613 mg $Mn(ac)_2.4H_2O$ was added in 25 mL binary solvent mixture (water : *n*-heptane = 3:1 v/v) and was brought to reflux (*ca.* 65−70°C) under stirring. After about 30 min, 20 µL of ammonium hydroxide was added and immediately after, 1 mL of preformed silver nanoparticles (0.25 mM) was added dropwise continuing few minutes to the solution under reflux. The refluxing was continued overall for 1.5 h. Upon addition of the silver colloid, the colour of the sol was, slowly, begun to change and finally, a brownish yellow colouration was seen at the end of the reaction. After that, the reaction mixture was cooled down to room temperature and stirring was continued overnight. By varying the size of silver nanoparticles, different sets of the nanocomposites could be achieved. The brownish yellow colour dispersion so obtained was washed thrice by centrifugation and

redispersion in distilled water. Finally, the as-obtained precipitate was dispersed in distilled water and stored in the vacuum desiccator. Manganese oxide nanoparticles were synthesised following the same procedure devoid of addition of any silver nanoparticles.

4.2.2.3. Gas Sensing Measurements

The as-prepared Mn_3O_4 and Mn_3O_4−Ag powders were mixed with a suitable amount of isopropanol to form a paste. The pastes were, then, coated (coating thickness ~ 100 µm) onto alumina tubes (length 4 mm, outer diameter 2 mm and thickness 0.5 mm) on which two gold electrodes and platinum wires have, already, been placed at each end. A detail of the experimental set-up has been described elsewhere[95,96] The nanocomposites were, initially, aged at 300 °C for 72 h to achieve the desired stability before the sensitivity measurements. The sensors were, then, exposed to air and in ethanol vapour of various concentrations ranging from 5 to 100 ppm. The gas response of the sensor was measured after achieving a stable response upon exposure to the targeted gas. The electrical resistance of the thin film sensors in air (R_a) and in the presence of gas mixtures (R_g) was measured to evaluate the gas response (S). The gas response (S) is calculated using the following equation,

$$S(\%) = \frac{(R_g - R_a)}{R_a} \text{X } 100 \qquad (4.4)$$

4.2.3. Results and Discussion

In the series of manganese oxides available in their different oxidation states, Mn_3O_4 is a unique mixed-valence oxide that adopts a tetragonally distorted spinel structure under ambient conditions[97]with a wide direct bandgap of 2.30 eV. On the other hand, silver particles, in the nanometer size regime, exhibit strong absorption in the visible region; the time-varying electric field of the electromagnetic radiation causes collective oscillation of the conduction electrons in metal nanoparticles with a resonance frequency, often coined as localised surface plasmon resonance (LSPR).[98]Under the experimental condition, seed-mediated epitaxial growth of manganese oxide occurs by alkaline hydrolysis of manganese precursor on preformed silver nanoparticles.

4.2.3.1. Absorption Spectroscopy

The changes in the optical characteristics of the as-prepared Mn_3O_4–Ag nanocomposites due to the evolution of manganese oxide onto the preformed size-selective silver nanoparticles have been elucidated through diffuse reflectance spectroscopy. The diffuse reflectance spectra of the Mn_3O_4−Ag NCs measured in the solid state are shown in Fig. 4.11. A closer inspection of the spectral features shows three well-defined regions: the first portion from 250 to 325 nm, the second from 325 to 500 nm, and the third one finishing at around 750 nm. The first portion is assigned to the allowed $O^{2-} \rightarrow Mn^{2+}$ and $O^{2-} \rightarrow Mn^{3+}$ charge-transfer transitions, and the last two can be reasonably related to d-d crystal-field transitions, $^3E_g(G) \leftarrow {}^3T_{1g}$, $^3A_{2g}(F) \leftarrow {}^3T_{1g}$, $^3A_{2g}(G) \leftarrow {}^3T_{1g}$, $^3T_{2g}(H) \leftarrow {}^3T_{1g}$, $^3T_{1g}(H) \leftarrow {}^3T_{1g}$, and $^3E_g(H) \leftarrow {}^3T_{1g}$, on octahedral Mn^{3+} species.[99]Moreover, in all sets of the nanocomposites, the second portion shows a maximum in the region of ~400 nm, that arises due to the localised surface plasmon resonance of spherical silver nanoparticles.[100]The appearance of silver surface plasmon band reveals the presence of metallic silver in Mn_3O_4−Aghetero nanostructures. The color change is clearly seen before and after Mn_3O_4 conjugation to the silver nanoparticles as shown in the inset. The color of Mn_3O_4 NPs is brown and that of Ag NPs is yellow, while the resulting Mn_3O_4−Ag nanocomposites are yellowish brown. This suggests that the finally formed Mn_3O_4−Ag nanocomposites have inherited the colorimetric character of Mn_3O_4 nanoparticles.[101]

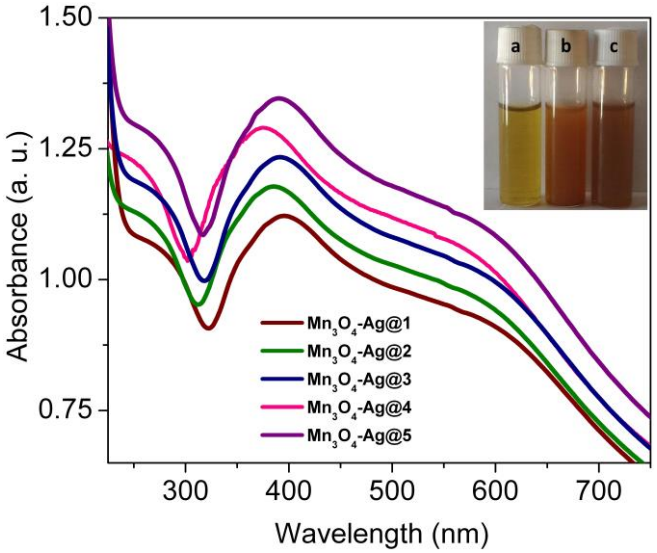

Fig.4.11. Solid state Absorbance spectra of the different sets of Mn_3O_4−Ag nanocomposites containing silver nanoparticles of different sizes. Inset shows the digital photograph of Ag NPs@3, Mn_3O_4 NPs, and Mn_3O_4−Ag@3 NCs exhibiting colour change upon formation of the nanocomposites.

4.2.3.2. Band Gap Engineering in Ag-Mn_3O_4 Nanocomposites

The band gap of semiconductors could be engineered for achieving desired physical properties.[102] It has been established that the manipulating and guiding photons at the nanoscale is possible with the assistance of interdigitated plasmonics. Moreover, in semiconductor–metal composites, the photoinduced charge carriers are trapped by the noble metal particles and become able to promote the interfacial charge–transfer processes.[103] The direct band gap energy (E_g) of the Mn_3O_4–Ag NCs could be determined by fitting the absorption data to the direct band gap transition equation as,$(\alpha h\nu)^2 = A(h\nu - E_g)$, where, α is the absorption co-efficient, $h\nu$ the photon energy and A a constant. The absorption coefficient (α) is defined as: α =2.303 A/L c, where, A is the absorbance of the sample, c the loading of sample (g L^{-1}), L the path length (= 1 cm). Fig. 4.12shows the plot of $(\alpha h\nu)^2$ as a function of photon energy (hν) of the as-synthesised pure Mn_3O_4 NPs and five different sets of Mn_3O_4–Ag NCs. Although, the band gap of pure Mn_3O_4 NPs appears as3.08 eV, the band gap values are calculated as 2.27, 2.50,

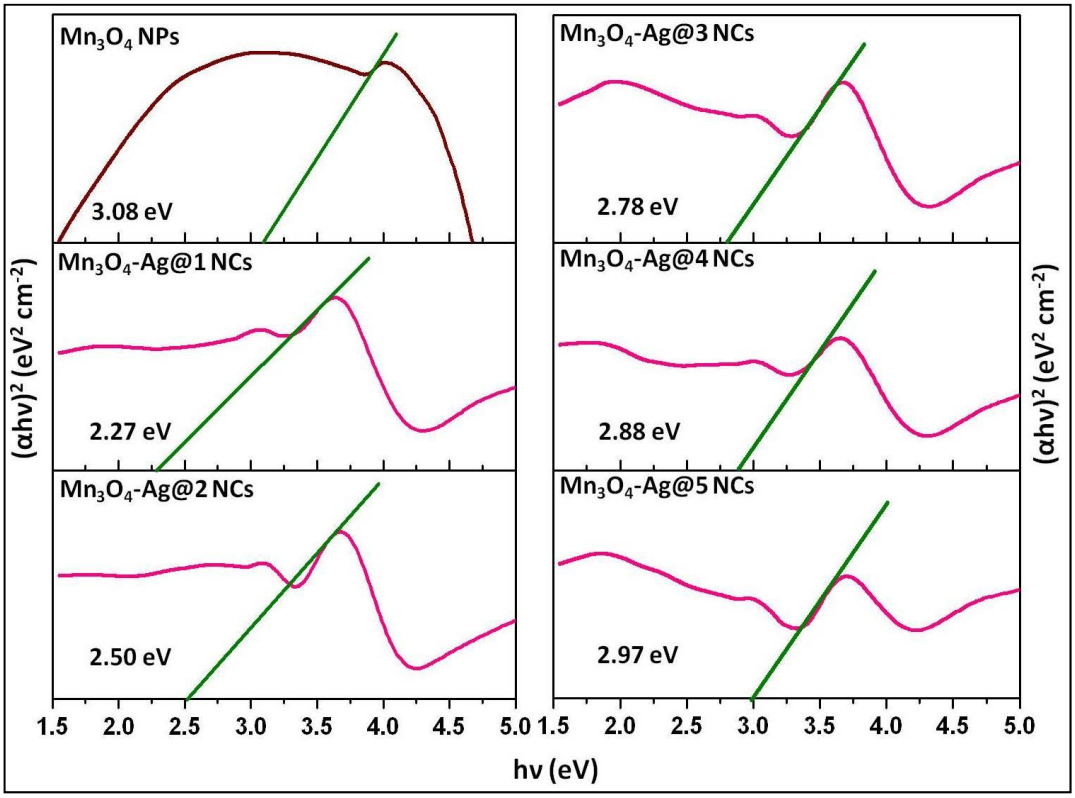

Fig. 4.12. Tauc's plot for the estimation of band gap energy of Mn_3O_4 NPs and different sets of Mn_3O_4−Ag nanocomposites.

2.78, 2.88 and 2.97 eV for Mn_3O_4–Ag nanocomposites containing 2, 5, 10, 15 and 20 nm silver particles, respectively. It is, therefore, apparent that the band gap decreases with decrease in size of the silver nanoparticles in the composites that arises due to the high surface energy of the small metallic particulates.[104]

4.2.3.3. Morphology, Composition and Crystallinity of the Mn_3O_4 NPs and Mn_3O_4–Ag NCs

The structural morphology, composition and crystallinity of the as-synthesised Mn_3O_4−Ag nanocomposites have been elucidated by various characterisation techniques as shown in Fig. 4.13. Low resolution transmission electron micrograph of Mn_3O_4 (panel a) shows that the particles are tetragonal with average diameter 25 ± 10 nm. Representative transmission electron micrograph of Ag@3 (panel b) shows that the particles are spherical with average diameter 10 ± 1.0 nm. The corresponding TEM characterisations of Mn_3O_4−Ag@3 (panel c) shows several spherical inclusions within tetragonal morphology with an enlarged diameter of 35 ± 15 nm that can be attributed to the anchoring of the Ag nanoparticles in the Mn_3O_4 lattices. It is also observed that the diameter of the nanocomposites does not increase, considerably, with increase in the

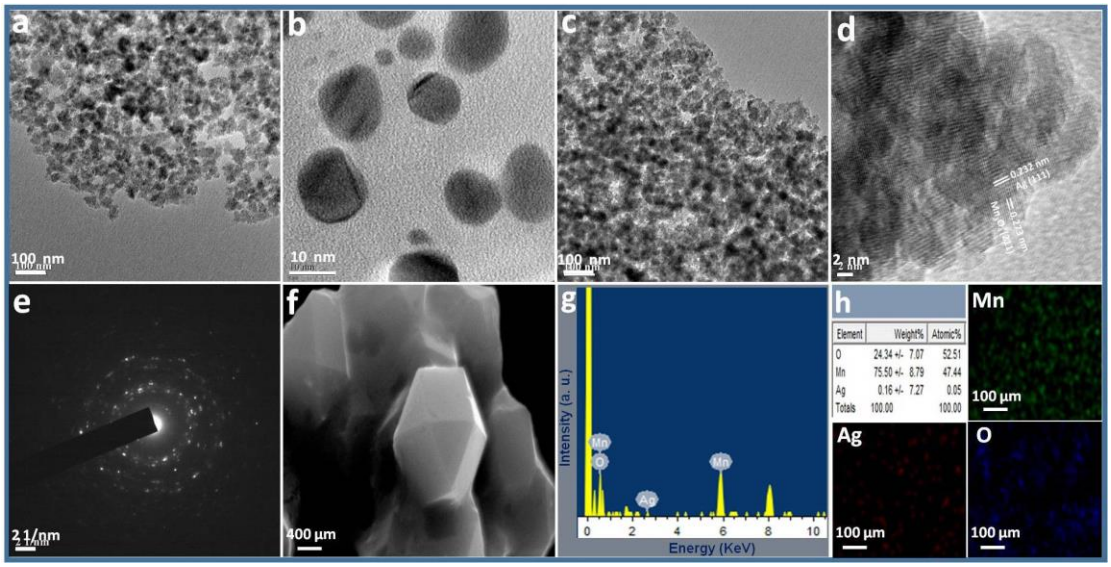

Fig. 4.13.(a, b, c) Representative transmission electron micrographs of Mn_3O_4 NPs, Ag NPs and Mn_3O_4-Ag@3 NCs; (d) high resolution transmission electron micrograph, (e) selected area electron diffraction pattern, (f) representative field emission scanning electron micrograph, (g) energy dispersive X-ray spectrum and (h) elemental mapping of Mn_3O_4-Ag@3 NCs.

diameter of the silver particles; however, the spherical inclusion within the tetragonal morphology remains unaltered in all sets of nanocomposites. High resolution transmission electron micrograph of Mn_3O_4−Ag@3 (panel d) exhibits excellent crystallinity and clear lattice fringes with d-spacing of 0.249 nm corresponding to the distance between the (211) planes of the Mn_3O_4 tetragonal crystal lattice[105] and 0.232 belonging to the (111) plane of fcc Ag in the nanocomposites.[106] The corresponding selected area electron diffraction pattern of Mn_3O_4−Ag@3 nanocomposites (panel e) shows the appearance of polycrystalline-like diffractions that are consistent with reflections (112), (103),(211), (220), (105) and (224) planes corresponding to the tetragonal Mn_3O_4 structure along with (111), (200) and (220) diffraction lines of Ag which reveals the crystallographic orientations for both Mn_3O_4 and Ag in the nanocomposites.[107] Field emission scanning electron micrograph of Mn_3O_4−Ag@3 (panel f) shows the presence of smooth and roughly uniform tetragonal agglomerates that are arising due to the soft aggregation of the nanocomposites on the silicon wafer.[107] The representative energy dispersive X-ray spectrum of Mn_3O_4−Ag@3 nanocomposites (panel g) indicates that the particles are composed of Mn, O and Ag elements, that points out to the formation of Mn_3O_4 during the epitaxial growth on the silver particles.[107] The distribution of elements present in the as-synthesised Mn_3O_4−Ag@3 composites has been convoluted from the elemental mapping and the presence of green, red and blue regions corresponds to Mn, Ag and O elements, respectively. Thus, the elemental distribution also provides evidence to the successful preparation of binary composites from the individual components.[107]

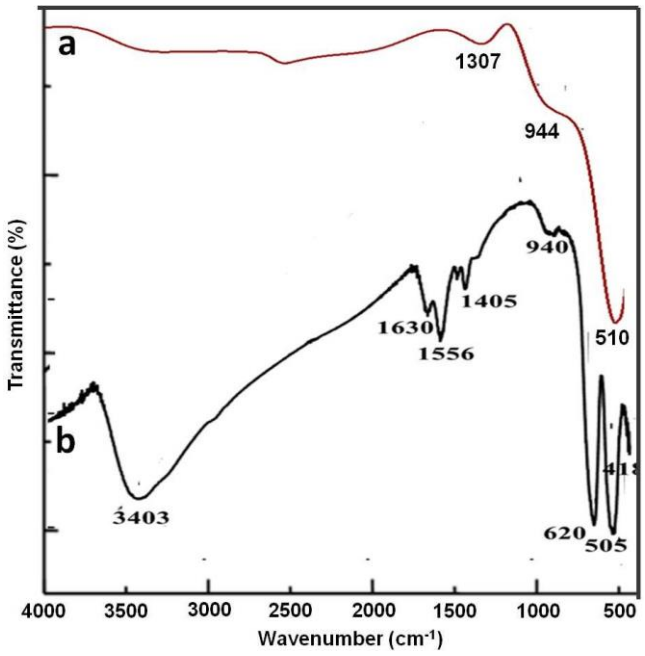

Fig. 4.14. Fourier transform infrared spectrum of (a) Mn_3O_4 NPs and (b) Mn_3O_4–Ag@3 NCs.

4.2.3.4. Fourier Transform Infrared Spectroscopy ofMn_3O_4 NPs andMn_3O_4−Ag@3NCs

Fourier transform infrared spectra of Mn_3O_4NPs andMn_3O_4−Ag@3NCs are shown in Fig. 4.14.The spectrum of Mn_3O_4 NPs (trace a) shows a lower region band at 510 cm^{-1}, that can be assigned to Mn–O stretching vibrations,[108] the appearance of an additional band at 944 cm^{-1} is related to the stretching vibration of Mn–O–Mn species.[108]Moreover, the other absorption band at 1307 cm^{-1} corresponds to the C–O stretching frequency due to adsorbed acetate counter ions.[109] Upon conjugation with the silver nanoparticles (trace b), a doublet of peaks at 505 and 418 cm^{-1} could be assigned to Mn–O and Ag–O stretching vibrations, respectively.[110] In addition, the presence of additional bands at 620 cm^{-1} and 940 cm^{-1} could be ascribed to the stretching vibration of Mn–O and Mn–O–Mn species, respectively, in the environment of nanocomposites. The other absorption bands at 1405 and 1556 could be attributed to the asymmetric and symmetric COO^- stretching vibrations of citrate and acetate chemisorption, respectively, which, probably, accounts for the stabilisation of the nanocomposites.[109] The appearance of a broad band at 3403 cm^{-1} and a narrow band at 1630 $cm^{-1}$are seen due to the stretching and bending modes of O−H groups, that reveal the existence of a small amount of water physisorbed and/or chemisorbed by the nanocomposites.[108]

4.2.3.5. X-ray Diffraction Patterns of Mn_3O_4 NPs and Ag-Mn_3O_4 NCs

The phase identification of the as-prepared Mn_3O_4 NPs andMn_3O_4−Ag@3NCs has been illustrated from the characteristic X-ray diffraction patterns as shown in Fig. 4.15. Trace a represents the X-ray diffraction features of

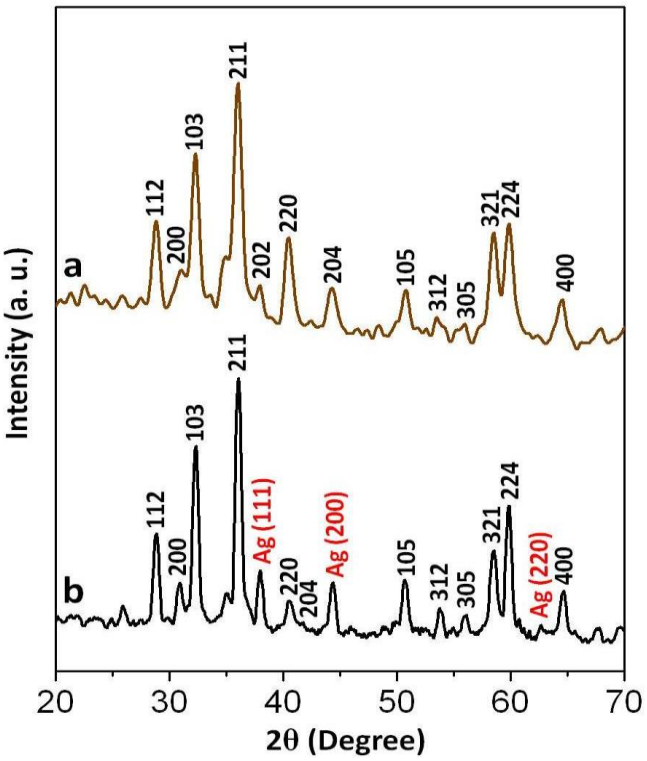

Fig. 4.15. X-ray diffraction pattern of (a) Mn_3O_4 NPs and (b) Mn_3O_4–Ag@3 NCs.

manganese oxide nanoparticles; the diffraction peaks located at 29.05, 31.04, 32.5, 36.08, 36.5, 44.3, 51.1, 53.91, 58.5, 60.1, and 64.7° can, perfectly, be indexed to (112), (200), (103), (211), (202), (220), (105), (312), (321), (224), and (400) crystallographic planes of the single-phase tetragonal Mn_3O_4 spinel structure corresponding to lattice constants, a = b = 5.7592 and c = 9.4663 Å and space group $I4_{I/amd}$, which are consistent with the standard values of bulk Mn_3O_4 (JCPDS# 24-0734).[111]However, no characteristic peaks of any impurity phases or other MnO_x phases could be traced in the XRD pattern which is indicative of high purity of the as-prepared Mn_3O_4 nanoparticles. Upon conjugation with the silver nanoparticles (trace b), in addition to the intrinsic peaks of tetragonal Mn_3O_4, additional diffraction peaks at *ca.* 38.0°, 44.1° and 64.3° corresponding to the diffraction lines of (111), (200) and (220), respectively, are observed that can be indexed as the face-centred cubic phase of Ag(JCPDS# 87-0597).[107]These results indicate that the prepared nanocomposites consist of tetragonal and face-centred cubic structures of Mn_3O_4 and Ag, respectively and the presence of preformed Ag favours the formation of an ordered and single phase of Mn_3O_4 in the nanocomposites.[107,111]

4.2.3.6. Raman Spectrum of Mn_3O_4–Ag@3 Nanocomposites

Raman spectroscopy has been used for the sensitive detection of optical phonon modes related to vibrational properties of the nanocomposites. Fig. 4.16 shows the room temperature Raman scattering spectrum of Mn_3O_4–Ag@3 nanocomposites in the 100−1000 cm^{-1} spectralrange; in the present experiment, the samples were excited by the 488 nm line (2.55 eV) of Ar^{+} laser. The spectrum exhibits three phonon peaks: E_g symmetry mode at 293 cm^{-1}, T_{2g} symmetry mode at 353 cm^{-1} and A_{1g} symmetry 'breathing' mode at 641 cm^{-1} of Mn_3O_4.[112] The

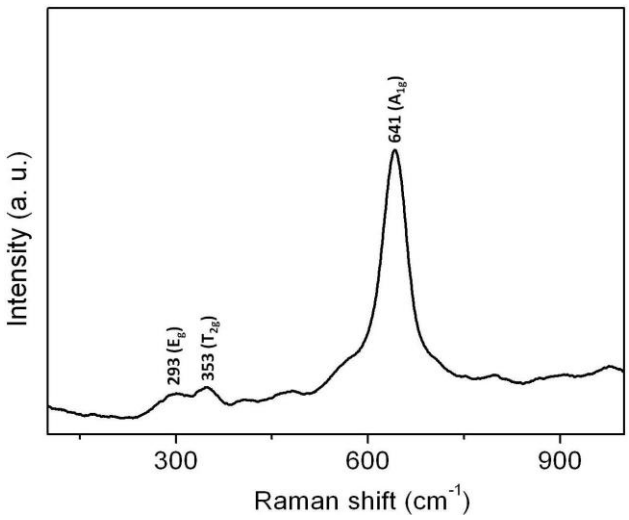

Fig.4.16. Raman Spectrum of Mn_3O_4–Ag@3 Nanocomposites

strong peak located at 641 cm^{-1} is the characteristic of tetragonal Mn_3O_4 spinel, corresponding to the Mn−O stretching vibration of divalent manganese ions associated with the tetrahedral coordination.[113]

4.2.3.7. Cyclic voltammograms of Mn_3O_4 NPs, Ag NPs and Mn_3O_4-Ag@3 NCs

Cyclic voltammograms of as-prepared Mn_3O_4 NPs, Ag NPs and representative Mn_3O_4–Ag@3 NCs (0.01 M) in 0.1 M KCl solution using Ag/AgCl as a reference electrode and Pt electrodes as working and counter electrodes are shown in Fig. 4.17. It has been noted that pure Mn_3O_4 shows the anodic current (I_a) as 2.02 and cathodic current (I_c) as 3.28 μA at the potentials of 0.56 and 0.83 V, respectively, while Ag NPs exhibit only cathodic current (I_c) as 2.41 μA at a potential 0.83 V. On the contrary, the spectrum of Mn_3O_4–Ag@3 NCs shows high anodic current (I_a) as 5.22 and cathodic current (I_c) as 10.50 μA at the potentials of 0.56 and 0.80 V, respectively.[114] It is known that the differences in the flow of current are related to the differences in the rate of electron transfer at the interface of the electrodes that reflect the difference in charge densities.[114]The highest current density values in case of Mn_3O_4–Ag nanocomposites indicates highest rate of electron transfer in the conjugates than the individual components.[114] Moreover, the anodic peak potential (E_{pa}) of the Mn_3O_4 NPs, Ag NPs, and Mn_3O_4−Ag NCs is measured to be 0.59, 0.65, and 0.56 V, respectively. From these data, it is noted that the anodic peak potential is in the order of Ag NPs > Mn_3O_4 NPs > Mn_3O_4−Ag NCs, that is, the anodic/oxidation potential is less in composites as compared to Mn_3O_4 NPs while high with respect to Ag NPs. It, therefore, indicates that the charge transfer takes place from Mn_3O_4 to Ag, which reduces the potential differences between the two components in Mn_3O_4−Ag NCs.[115]

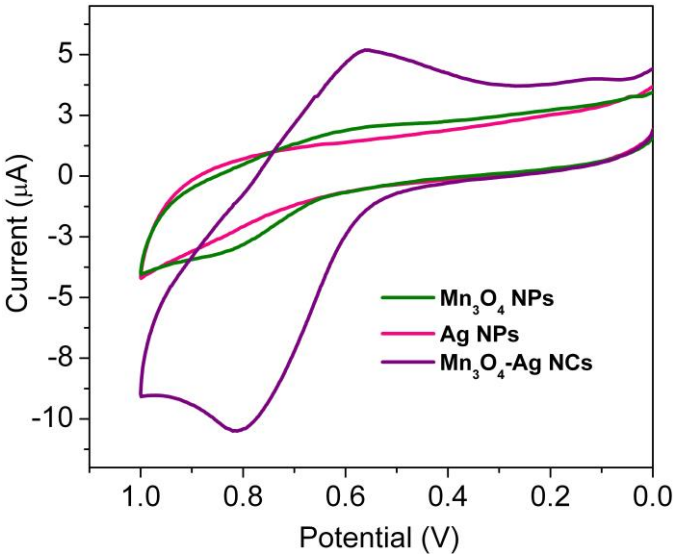

Fig. 4.17. Cyclic voltammograms of Mn_3O_4 NPs, Ag NPs and Mn_3O_4-Ag@3 NCs.

4.2.3.8. Thermogravimetric Analysis of Mn_3O_4–Ag@3 Nanocomposites

Thermogravimetric analysis presented in Fig. 4.18 displays weight losses of the representative Mn_3O_4–Ag@3 in two distinct regions. Initial weight loss of 7.3% below 190 °C is due to the removal of physically and/or chemically adsorbed water in the nanocomposites. The following major weight loss of 31.6% in the temperature range of 250−330 °C, could be attributed to the decomposition of citrate and acetate counter ions, responsible for the stabilisation of the nanocomposites.[116]

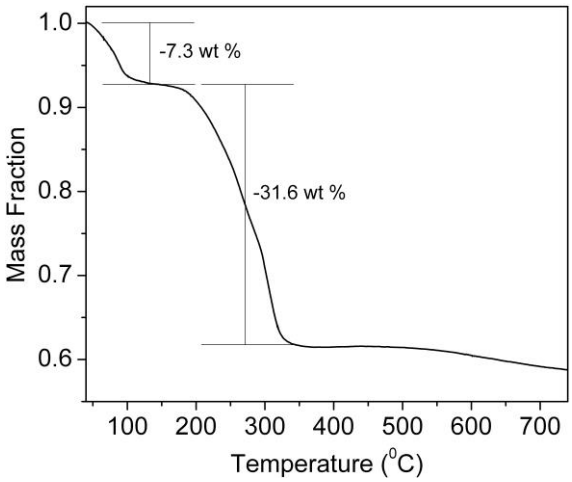

Fig. 4.18. TGA weight loss pattern of Mn_3O_4–Ag@3 nanocomposites.

4.2.3.9. Sensing of Volatile Organic Compounds (VOCs) byMn_3O_4 Nanoparticles and Mn_3O_4–Ag Nanocomposites

Semiconducting metal oxides at the nanoscale dimension have received considerable attention for gas sensing applications, owing to the advantages of synthesising from earth abundant materials, ease of synthesis, high sensitivity and selectivity, and excellent reversibility.[74,75] The sensing behaviour of nanomaterials is based on the principle of adsorption/desorption of test gases on their surfaces that leads to electrochemical changes, catalytic combustion

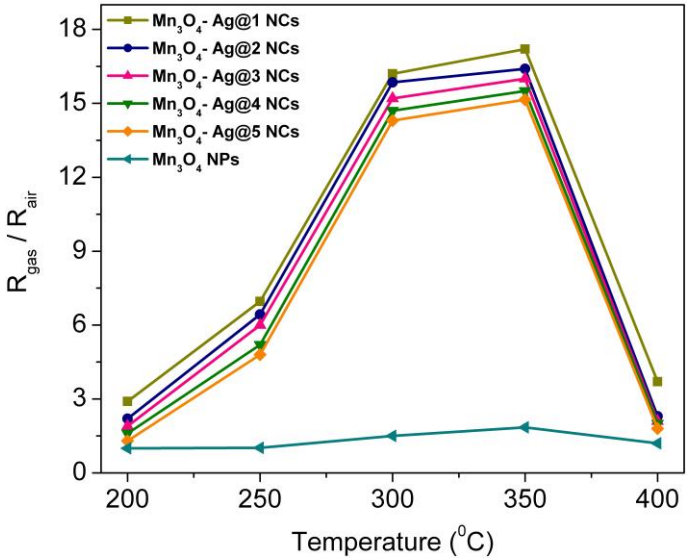

Fig. 4.19. Gas sensing response curves ofMn_3O_4-Ag@1 nanocomposite sensors as a function of time at different operating temperatures.

or resistance modulation of these materials.[117,118] Based on these conceptives, we have studied the sensing performance of the earth abundant manganese oxides by sensitization with catalytic active silver nanoparticles.[84] The gas sensitivity of the Mn_3O_4 NPs and Mn_3O_4−Ag NCs sensors was tested as a function of time. Fig. 4.19.shows the gas-sensing performance of Mn_3O_4-Ag@1 nanocomposite sensors for a fixed concentration of 50 ppm ethanol gas. It is seen that gas sensing response is low at operating temperature of 250 ^oC, reaches maximum at 350 ^oC and decreases drastically upon further increase of temperature. These observations are in conformity with the trend of increase-maximum-decay to various gases with increase in temperature,[120] and can be explained by considering the activation energy of the chemical reaction (sensing of gas molecule). At low temperatures, the response is governed by the speed of chemical reaction while at high temperatures, it is dominated by the speed of diffusion of gas molecules,[121] at intermediate temperatures, the speed of the two processes becomes equal and therefore, the response becomes maximum. It is, therefore, clear that the operating temperature is one of the important parameters that determine the sensitivity of the gas sensor. From the response curve, two important parameters, *viz*., response and recovery time has been calculated as ~5 and 24 s, respectively, which reveals the response and recovery of the sensor is quite fast.Now, we have studied the comparative response ofMn_3O_4 NPs and Mn_3O_4–Ag NCs containing silver nanoparticles of five different sizes towards the sensing of 50 ppm ethanol gas in a variable temperature probe station as shown in Fig. 4.20. It is observed that deposition of Ag on the Mn_3O_4 surface,

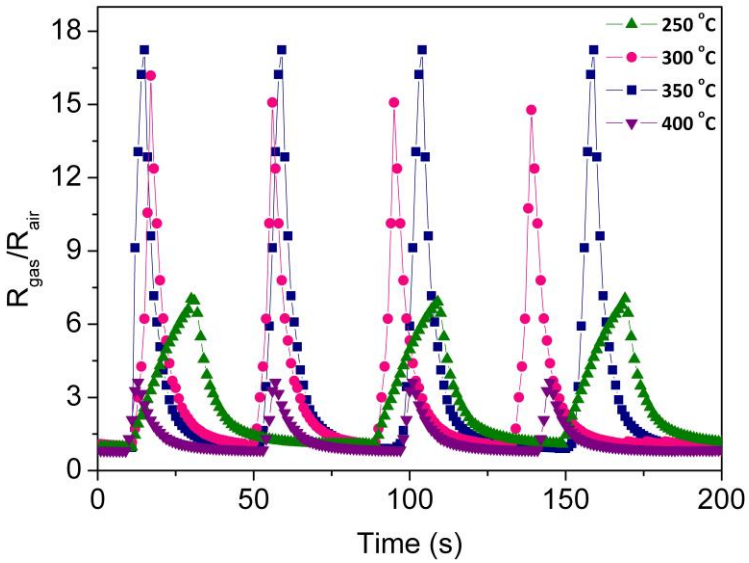

Fig. 4.20. Profiles showing the comparative sensory responses of Mn_3O_4 NPs and five different sets Mn_3O_4–Ag NCs containing silver nanoparticles of five different sizes as a function of operating temperature.

promotes the sensory response to oxidising gases by more than 10−15 times. The improved catalytic activity upon addition of silver in the manganese oxide matrix due to reduction in the band gap has been presented in Scheme 4.3. Moreover, it is noted that sensory response decreases with increase in size of the silver particles in the nanocomposites. These observations are due to the fact that, there is a formation of p-n type hetero-junction with relatively low band gap and become narrower with decrease in size of the silver particles in the composites.[119,120]To investigate the reproducibility of proposed method, all the experiments have been repeated thrice under similar experimental conditions. It is seen that the all the sets of nanocomposites exhibit dramatic

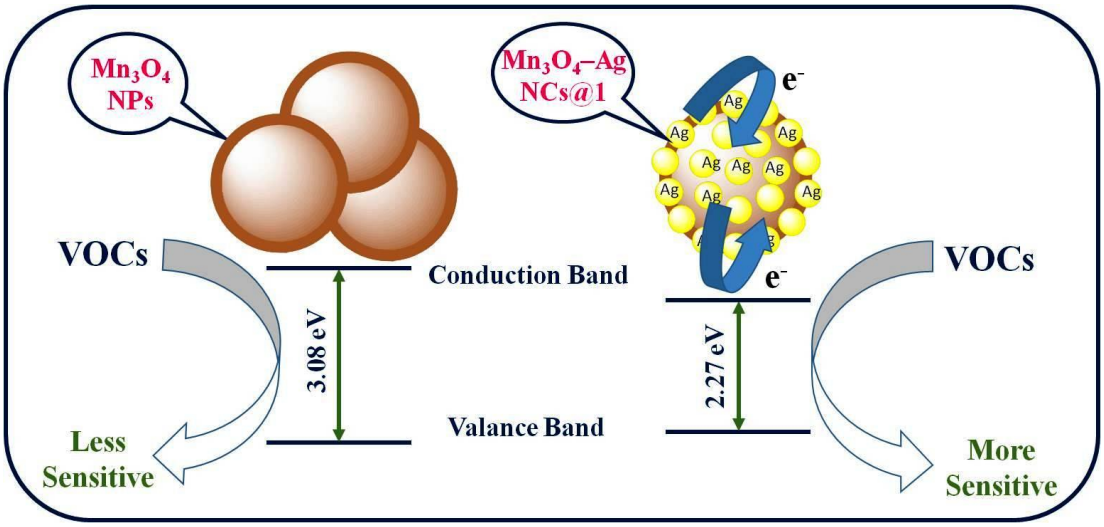

Scheme 4.3. Schematic presentation of the reduction of the band gap and improved sensory activity in the presence of Mn_3O_4–Ag nanocomposites.

improvement in sensitivity toward VOCs than that of bare metal oxide nanoparticles which indicates that conjugation of silver adds functionality to the Mn_3O_4 matrix. This is due to the enhanced dissociation of the molecular adsorbate on the catalytic silver nanoparticle surfaces and the subsequent diffusion of the ensuing atomic species to the manganese oxide surface.[84]Moreover, the nanocomposites possess decreased sensory responses for recognizing ethanol with increase silver nanoparticle size; this is consistent with the lowering of band gaps with decrease in size of the metallic particles in Mn_3O_4−Ag composites.[121]

Fig. 4.21. shows the histogram of the sensory response of Mn_3O_4–Ag@1 NCs towards methanol, ethanol, acetone, carbon monoxide, methane and *n*-butane. It is seen that the nanocomposite sensors are selective to ethanol in comparison to the other volatile organic compounds. To check the stability of the sensors, base resistance and response of Mn_3O_4-Ag@1 nanocomposites were tested for a period of four weeks under similar conditions. It is observed that the sensitivity does not decrease, considerably, during this time period indicating stability and reliability of the nanocomposite sensors for the detection of volatile organic compounds.

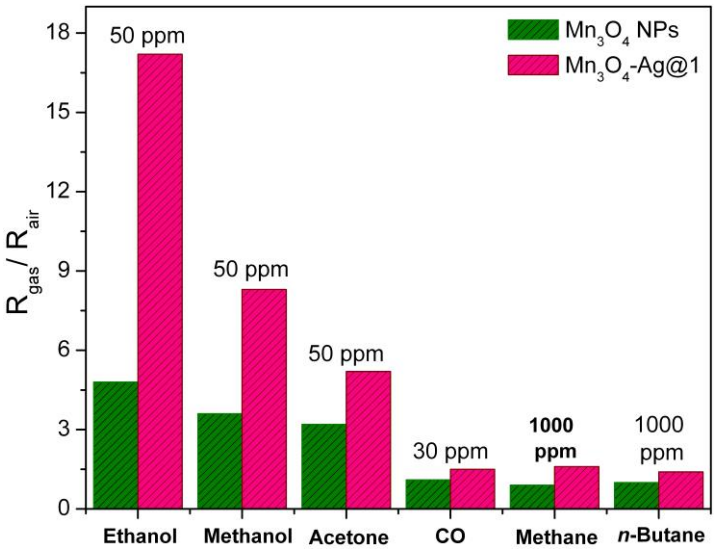

Fig. 4.21. Histogram showing the sensitivity of Mn_3O_4-Ag@1 nanocomposite sensors upon exposure to different volatile organic compounds.

4.2.4. Conclusion

In conclusion, Mn_3O_4−Ag nanocomposites have been synthesised by seed-mediated epitaxial growth of manganese oxide on the surface of preformed silver nanoparticles at the liquid-liquid interface under mild refluxing condition. The morphology of the nanocomposites has been varied by variation of the size of the silver nanoparticles. The morphological characterisations by several spectroscopic and microscopic techniques ensured the formation of Mn_3O_4−Ag consisting of single phase tetragonal Mn_3O_4 spinel and fcc Ag structures in the nanocomposites. Upon conjugation of manganese oxide to silver nanoparticles, charge transfer takes place from Mn_3O_4 to Ag in Mn_3O_4−Ag NCs. The band gap of the nanocomposites has been reduced with decrease in increase in size of the silver particles in the nanocomposites. The as-synthesised nanocomposites have been exploited towards the sensing of volatile organic compounds and under the optimized conditions, the nanocomposite sensors have been found to be selective to ethanol. Thus, the semiconducting metal oxide nanostructures impregnated with plasmonic metal nanoparticles offer functional heterogeneous catalysts, owing to the synergetic effects of Ag and Mn_3O_4in the nanocomposites. The sensory activity of these nanocomposites could be controlled by manipulating the band gap by variation of the size of the metallic components and may hold great promise for the development of effective ethanol sensors.

4.3. References

1. J. K. Hurst, *Science*, 2010, **328**, 315–316.
2. S. Trassati, In *The Electrochemistry of Novel Materials* (J. Lipkowski and P. N. Ross, Eds.) Wiley-VCH, Weinheim, 1994, pp.207–296.
3. S. M. Barnett, K. I. Goldberg and J. M. Mayer, *Nature Chem.*, 2012, **4**, 498−502.
4. R. Eisenberg and H. B. Gray, *Inorg. Chem.*, 2008, **47**, 1697–1699.
5. J. H. Alstrum-Acevedo, M. K. Brennama and J. T. Meyer, *Inorg. Chem.*, 2005, **44**, 6802–6827.
6. F. Liu, J. J. Concepcion, J. W. Jurss, T. Cardolaccia, J. L. Templeton and J. T. Meyer, *Inorg. Chem.*, 2008, **47**, 1727–1752.
7. M. G. Walter, E. L. Warren, J. R. McKone, S. W. Boettcher, Q. Mi, E. A. Santori and N. S. Lewis, *Chem. Rev.*, 2010, **110**, 6443-6473.
8. N. S. Lewis, G. Crabtree, A. J. Nozik, M. R. Wasielewski and A. P. Alivisatos, In *Basic Research Needs for Solar Energy Utilization; Department of Energy*, Washington DC, 2005.
9. J. P. McEvoy and G. W. Brudvig, *Chem. Rev.*, 2006, **106**, 4455–4483.
10. M. Grätzel, *Acc. Chem. Res.*, 1981, **14**, 376–384.
11. N. S. Porter, H. Wu, Z. Quan and J. Fang, *Acc. Chem. Res.*, 2013, **46**, 1867–1877.
12. T. Nakagawa, N. S. Bjorge and R. W. Murray, *J. Am. Chem. Soc*., 2009, **131**, 15578–15579.
13. L. Duan, F. Bozoglian, S. Mandal, B. Stewart, T. Privalov, A. Llobet and L. Sun, *Nature Chem.*, 2012, **4**, 418–423.
14. M. J. Kenney, M. Gong, Y. Li, J. Z. Wu, J. Feng, M. Lanza and H. Dai, *Science*, 2013, **342**, 836–840.
15. J. Z. McAlpin, T. A. Stich, C. A. Ohlin, Y. Surendranath, D. G. Nocera, W. H. Casey and R. D. Britt, *J. Am. Chem. Soc.*, 2011, **133**, 15444–15452.
16. W. C. Ellis, N. D. McDaniel, S. Bernhard and T. J. Collins, *J. Am. Chem. Soc.*, 2010, **132**, 10990–10991.
17. S. M. Barnett, K. I. Goldberg and J. M. Mayer, *Nature Chem.*, 2012, **4**, 498–502.
18. N. S. Lewis, *Science*, 2007, **315**, 798−801.

19. I. Djerdj, D. Arčon, Z. Jagličić and M. Niederberger, *J. Phys. Chem. C*, 2007, **111**, 3614-3623.
20. E. Grootendorst, Y. Verbeek, and V. Ponce, *J. Catal.*, 1995, **157**, 706–712.
21. C. −C. Hu, Y. -T. Wu and K. −H. Chang, *Chem. Mater.*, 2008, **20**, 2890–2894.
22. S. K. Ghosh, J. Kang, M. Inokuchi and N. Toshima, *Appl. Catal., A* 2014, **464-465**, 225-232.
23. M. Haruta, *Faraday Discussions*, 2011, **152**, 11–32.
24. In *Metal Nanoclusters in Catalysis and Materials Science: The Issue of Size Control* B. Corain, *G.* Schmid and N. Toshima, Eds., Elsevier, Amsterdam 2008.
25. G. C. Dismukes, R. Brimblecombe, G. A. N. Felton, R. S. Pryadun, J. E. Sheats, L. Spiccia and G. F. Swiegers, *Acc. Chem. Res.*, 2009, **42**, 1935-1943.
26. Y. Gorlin and T. F. Jaramillo, *J. Am. Chem. Soc.*, 2010, **132**, 13612–13614.
27. Y. Gorlin, C. –J. Chung, J. D. Benck, D. Nordlund, L. Seitz, T. –C. Weng, D. Sokaras, B. M. Clemens and T. F. Jaramillo, *J. Am. Chem. Soc.*, 2013, **135**, 16977-16987.
28. M. M. Najafpour, A. N. Moghaddam, H. Dau and I. Zaharieva, *J. Am. Chem. Soc.*, 2014, **136**, 7245–7248.
29. M. Wiechen, I. Zaharieva, H. Dau and P. Kurz, *Chem. Sci.*, 2012, **3**, 2330-2339.
30. A. Singh, R. K. Hocking, S. L. -Y. Chang, B. M. George, M. Fehr, K. Lips, A. Schnegg and L. Spiccia *Chem. Mater.*, 2013, **25**, 1098–1108.
31. M. Wiechen and L. Spiccia, *ChemCat Chem.*, 2014, **6**, 439−441.
32. M. Wiechen, M. M. Najafpour, S. I. Allakhverdiev and L. Spiccia, *Energy Environ. Sci.*, 2014, **7**, 2203−2212.
33. D. M. Robinson, Y. B. Go, M. Mui , G. Gardner, Z. Zhang, D. Mastrogiovanni, E. Garfunkel, J. Li, M. Greenblatt and G. C. Dismukes *J. Am. Chem. Soc.*, 2013, **135**, 3494–3501.
34. A. Iyer, J. Del-Pilar, C. K. King'ondu, E. Kissel, H. F. Garces, H. Huang, A. M. El-Sawy, P. K. Dutta and S. L. Suib *J. Phys. Chem. C*, 2012, **116**, 6474–6483.
35. G. Frens, *Nature*, 1973, **241**, 20−22.
36. M. Ali, S. K. Pal, H. Rahaman and S. K. Ghosh, *Soft Matter*, 2014, **10**, 2767−2774.

37. A. Vázquez-Olmos, R. Redón, A. L. Fernández and J. M. Saniger, *Appl. Phys. A,* 2005, **81**, 1131−1134
38. W. S. Kijlstra, E. K. Poels, A. Bliek, B. M. Weckhuysen and R.A. Schoonheydt, *J. Phys. Chem. B,* 1997, **101**, 309–316
39. K. S. Kim and N. Winograd, *Chem. Phys. Lett.*, 1975, **30**, 91–95.
40. X. Tanga, J. Li and L. S. Hao, *J. Appl. Catal. B*, 2010, **99**, 156–162.
41. T. Ahmad, K. V. Ramanujachary, S. E. Lofland and A. K.Ganguli, *J. Mater. Chem.*, 2004, **14**, 3406–3410.
42. Y. Tang, W. Cheng *Langmuir*, 2013, **29**, 3125−3132.
43. T. Nakagawa, C. A. Beasley and R. W. Murray *J. Phys. Chem. C*, 2009, **113**,12959-12961.
44. G. Li, Z. Tang, *Nanoscale*, 2014, **6**, 3995-4011.
45. F. W. Lytle, P. S. P. Wei, R. B. Greegor, G. H. Via and J. H. Sinfelt, *J. Chem. Phys.*, 1979, **70**, 4849-4855.
46. A. L. Ankudinov, J. J. Rehr, J. J. Low and S. R. Bare, *J. Chem. Phys.*, 2002, **116**, 1911−1919.
47. E. Yeager, *Electrochim. Acta*, 1984, **29**, 1527−1537.
48. M. M. Schubert, S. Hackenberg, A. C. van Veen, M. Muhler, V. Plzak and R. J. Behm, *J. Catal.*, 2001, **197**, 113–122.
49. L. M. Molina and B. Hammer, *Phys. Rev. Lett.*, 2003, **90**, 206102 1–4.
50. J. D. Benck, Z. Chen, L. Y. Kuritzky, A. J. Forman and T. F. Jaramillo, *ACS Catal.*, 2012, **2**, 1916−1923.
51. C. C. Chusuei and D. W. Goodman, In *Encyclopedia of Physical Science and Technology*; 3rd ed.; Robert, A. M., Eds.; Academic Press, New York, 2003, pp. 921−938.
52. V. M. −W. Huang, V. Vivier, M. E. Orazem, N. Pébère and B.Tribollet, *J. Electrochem. Soc.*, 2007, **154**, C99−C107.
53. D. K. Zhong and D. R. Gamelin, *J. Am. Chem. Soc.*, 2010, **132**, 4202–4207.
54. C. −C. Hu, Y. −T. Wu, K. −H. Chang, *Chem. Mater.*, 2008, **20**, 2890–2894.
55. J. −H. Park, A. H. Goldstein, J. Timkovsky, S. Fares, R. Weber, J. Karlik and R. Holzinger, *Science*, 2013, **341**, 9, 643−647.

56. S. J. Lawrence, *A Review of Selected Literature: Atlanta, Georgia, U. S. Geological Survey, Open-File Report*, 2006, **62**, 1338.
57. N. Queralto, A. N. Berliner, B. Goldsmith, R. Martino, P. Rhodes and S. H. Lim, *J. Breath Res.*, 2014, **8**, 027112 1-13.
58. C. Wang, R. Dong, X. Wang, A. Lian, C. Chi, C. Ke, L. Guo, S. Liu, W. Zhao, G. Xu and E. Li, *Sci. Rep.*, 2014, **4**, 1−8.
59. G. Peng, U. Tisch, O. Adams, M. Hakim, N. Shehada, Y. Y. Broza, S. Billan, R. Abdah-Bortnyak, A. Kuten and H. Haick, *Nature Nanotechnology*, 2009, **4**, 669−673.
60. H. Lin, M. Jang and K. S. Suslick, *J. Am. Chem. Soc.*, 2011, **133**, 16786−16789.
61. Y. Y. Broza and H. Haick, *Nanomedicine*, 2013, **8**, 785−806.
62. F. Röck, N. Barsan and U. Weimar, *Chem. Rev*., 2008, **108**, 705–725.
63. S. H. Lim, L. Feng, J. W. Kemling, C. J. Musto and K. S. Suslick, *Nat Chem.*, 2009, **1**, 562–567.
64. R. A. Potyrailo and V. M. Mirsky, *Chem. Rev.,* 2008, **108**, 771–813.
65. B. Li, G. Sauvé, M. C. Iovu, M. Jeffries-EL, R. Zhang, J. Cooper, S. Santhanam, L. Schultz, J. C. Revelli, A. G. Kusne, T. Kowalewski, J. L. Snyder, L. E. Weiss, G. K. Fedder, R. D. McCullough and D. N. Lambeth, *Nano Lett.*, 2006, **6**, 1598–1602.
66. J. Yoon, S. K. Chae and J. –M. Kim, *J. Am. Chem. Soc.*, 2007, **129**, 3038–3039.
67. A. D. F. Dunbar, S. Brittle, T. H. Richardson, J. Hutchinson and C. A. Hunter, *J. Phys. Chem. B*, 2010, **114**, 11697–11702.
68. Y. Lu, Y. Chang, N. Tang, H. Qu, J. Liu, W. Pang, H. Zhang, D. Zhang and X. Duan, *ACS Appl. Mater. Interfaces*, 2015, **7**, 17893–17903.
69. Z. Li, Q. Zhao, W. Fan and J. Zhan, *Nanoscale*, 2011, **3**, 1646−1652.
70. C. Tudisco, M. E. Fragalà, A. E. Giuffrida, F. Bertani, R. Pinalli, E. Dalcanale, G. Compagnini and G. G. Condorelli, *J. Phys. Chem. C*, 2016, **120**, 12611–12617.
71. Y. Chang, N. Tang, H. Qu, J. Liu, D. Zhang, H. Zhang, W. Pang and X. Duan, *Sci Rep.*, 2016, **6**, 1-12.
72. Y. Masuda, T. Itoh, W. Shin and K. Kato, *Sci. Rep.*, 2015, **5**, 10122, 1−7.
73. H. Yamagiwa, S. Sato, T. Fukawa, T. Ikehara, R. Maeda, T. Mihara and M. Kimura, *Sci. Rep.*, 2014, **4**, 6247 1-6.

74. A. Tricoli, M. Righettoni and A. Teleki, *Angew. Chem., Int. Ed.*, 2010, **49**, 7632–7659.
75. S. Elouali, L. G. Bloor, R. Binions, I. P. Parkin, C. J. Carmalt and J. A. Darr, *Langmuir*, 2012, **28**, 1879–1885.
76. M. Kimura, R. Sakai, S. Sato, T. Fukawa, T. Ikehara, R. Maeda and T. Mihara, *Adv. Funct. Mater.*, 2012, **22**, 469–476.
77. G. G. Huang, C. –T. Wang, H. –T. Tang, Y. –S. Huang and J. Yang, *Anal. Chem.*, 2006, **78**, 2397–2404.
78. D. P. Volanti, A. A. Felix, M. O. Orlandi, G. Whitfield, D.-J. Yang, E. Longo, H. L. Tuller and J. A. Varela, *Adv. Funct. Mater.*, 2013, **23**, 1759–1766.
79. S. Piperno, M. Passacantando, S. Santucci, L. Lozzi and S. L. Rosa, *J. Appl. Phys.*, 2007, **101**, 124504–124504.
80. A. K. Nayak, R. Ghosh, S. Santra, P. K. Guhab and D. Pradhan, *Nanoscale*, 2015, **7**, 12460–12473.
81. H. Li, W. Xie, T. Ye, B. Liu, S. Xiao, C. Wang, Y. Wang, Q. Li and T. Wang, *ACS Appl. Mater. Interfaces*, 2015, **7**, 24887−24894.
82. L. Xu, R. Xing, J. Song, W. Xu and H. Song, *J. Mater. Chem. C*, 2013, **1**, 2174-2182.
83. R. Xing, L. Xu, J. Song, C. Zhou, Q. Li, D. Liu and H. W. Song, *Sci. Rep.*, 2015, **5**, 10717 1−14.
84. A. Kolmakov, D. O. Klenov, Y. Lilach, S. Stemmer and M. Moskovits, *Nano Lett.*, 2005, **5**, 667−673.
85. J. Fu, C. Zhao, J. Zhang, Y. Peng and E. Xie, *ACS Appl. Mater. Interfaces*, 2013, **5**, 7410–7416.
86. I. Djerdj, A. Denis, J. Zvonko and M. Niederberger, *J. Phys. Chem. C*, 2007, **111**, 3614–3623.
87. A. M. E. Raj, S. G. Victoria, V. B. Jothy, C. R. J. Wollschlager, M. Suendorf, M. Neumann, M. Jayachandran and C. Sanjeeviraja, *Appl. Surf. Sci.*, 2010, **256**, 20−29.
88. Z. –J. Jiang, C. –Y. Liu and L. –W. Sun, *J. Phys. Chem. B*, 2005, **109**, 1730–1735.
89. J. Chen, X. Tang, J. Liu, E. Zhan, J. Li, X. Huang and W. Shen, *Chem. Mater.*, 2007, **19**, 4292–4299.

90. L. Wu, F. Xu, Y. Zhu, A. B. Brady, J. Huang, J. L. Durham, E. Dooryhee, A. C. Marschilok, E. S. Takeuchi and K. J. Takeuchi, *ACS Nano*, 2015, **9**, 8430–8439.
91. K. J. Takeuchi, S. L. Z. Yau, M. C. Menard, A. C. Marschilok, E. S. Takeuchi, *ACS Appl. Mater. Interfaces*, 2012, **4**, 5547–5554.
92. H. Huang, Y. Meng, A. Labonte, A. Dobley and S. L. Suib, *J. Phys. Chem. C*, 2013, **117**, 25352–25359.
93. W. Liu, C. Lu, X. Wang, R. Y. Tay and B. K. Tay, *ACS Nano*, 2015, **9**, 1528–1542.
94. S. Piperno, M. Passacantando, S. Santucci, L. Lozzi and S. L. Rosa, *J. Appl. Phys.*, 2007, **101**, 124504–124504
95. S. Chakraborty, A. Sen and H. S. Maiti, *Sens. Actuators B*, 2006, **115**, 610−614.
96. S. Kundu, P. K. Warran, Md. Mursalin and M. Narjinary, *J. Mater Sci: Mater. Elec*., 2015, **26**, 9865−9872.
97. M. Kim, X. M. Chen, X. Wang, C. S. Nelson, R. Budakian, P. Abbamonte, and S. L. Cooper, *Phys. Rev. B*, 2011, **84**, 174424-174433.
98. X. Liu, D. Li, X. Sun, Z. Li, H. Song, H. Jiang and Y. Chen,. *Sci. Rep.*, 2015, **5**, 12555 1−7.
99. R. J. O. Mossanek, G. Domínguez-Cañizares, A. Gutiérrez, M. Abbate, D. Díaz-Fernández and L Soriano, *J. Phys. Condens. Matter*, 2013, **25**, 495506 1−7.
100. D. D. Jr. Evanoff and G. Chumanov, *Chem. Phys. Chem.*, 2005, **6**, 1221**–**1231.
101. H. Yu, M. Chen, P. M. Rice, S. X. Wang, R. L. White and S. Sun, *Nano Lett.*, 2005, **5**, 379–382.
102. F. Wu, L. Tian, R. Kanjolia, S. Singamaneni and P. Banerjee, *ACS Appl. Mater. Interfaces* 2013, **5,** 7693−7697.
103. S. K. Dutta, S. K. Mehetor and N. Pradhan, *J. Phys. Chem. Lett.* 2015, **6**, 936−944.
104. Y. Dong, C. Feng, P. Jiang, G. Wang, K. Li and H. Miao, *RSC Adv.*, 2014,**4**, 7340–734.
105. P. Li, C. Nan, Z. Wei, J. Lu, P. Qing and Y. Li, *Chem. Mater.*, 2010, **22**, 4232–4236.
106. H. Liang, W. Wang, Y. Huang, S. Zhang, H. Wei and H. Xu, *J. Phys. Chem. C*, 2010, **114**, 7427–7431.
107. S. S. Acharyya, S. Ghosh, S. K. Sharma and R. Bal, *RSC Adv.*, 2015, **5**, 89879−89887.

108. S. Yang, H. Yang, H. Ma, S. Guo, F. Cao, J. Gong and Y. Deng, *Chem. Commun.*, 2011, **47**, 2619−2621.
109. K. Ito and H. J. Bernstein, *Can. J. Chem.* 1956, **34**, 170–178.
110. A. Mandal, S. Sekar, N. Chandrasekaran, A. Mukherjee and T. P. Sastry, *RSC Adv*., 2015, **5**, 15763-15771.
111. Z. –Y. Tian, P. M. Kouotou, N. Bahlawane and P. H. T. Ngamou, *J. Phys. Chem. C,* 2013, **117**, 6218–6224.
112. M. Kim, X. M. Chen, E. Fradkin, P. Abbamonte and S. L. Cooper, *Phys. Rev. Lett.*, 2010, **105**, 026402 1−3.
113. L. Malavasi, P. Galinetto, M. C. Mozzati, C. B. Azzonib and G. Flora, *Phys. Chem. Chem. Phys.*, 2002, **4**, 3876–3880.
114. Y. Wang, L. Cheng, F. Li, H. Xiong and Y. Xia, *Chem. Mater.*, 2007, **19**, 2095–2101.
115. G. –Q. Zhang, X. –G. Zhang and Y. –G. Wang, *Carbon*, 2004, **42**, 3097–3102.
116. H. Huang, S. Sithambaram, C.-H. Chen, C. K. Kithongo, L. Xu, A. Iyer, H. F. Garces and S. L. Suib, *Chem. Mater*., 2010, **22**, 3664−3669.
117. M. Kimura, R. Sakai, S. Sato, T. Fukawa, T. Ikehara, R. Maeda and T. Mihara, *Adv. Funct. Mater.*, 2012, **22**, 469–476.
118. G. G. Huang, C. –T. Wang,H. –T. Tang, Y. –S. Huang andJ. Yang,*Anal. Chem.*, 2006, **78**, 2397–2404.
119. H. Li, W. Xie, T. Ye, B. Liu, S. Xiao, C. Wang, Y. Wang, Q. Li and T. Wang, *ACS Appl. Mater. Interfaces*, 2015, **7**, 24887−24894.
120. G. Zhang, C. Li, F. Cheng, and J. Chen, *Sens. Actuators B*, 2007, **120**, 403–410.
121. X. Han, M. Jin, S. Xie, Q. Kuang, Z. Jiang, Y. Jiang, Z. Xie and L. Zheng, *Angew. Chem., Int. Ed.* 2009, **121**, 9180−9183.